

GRB 250702B: discovery of a gamma-ray burst from a black hole falling into a star

Eliza Neights ^{1,2}★† Eric Burns ³★† Chris L. Fryer ⁴, Dmitry Svinkin ⁵, Suman Bala ⁶, Rachel Hamburg ⁶, Ramandeep Gill ^{7,8}, Michela Negro ³, Megan Masterson ⁹, James DeLaunay ^{10,11}, David J. Lawrence ¹², Sophie E. D. Abrahams ¹³, Yuta Kawakubo ¹⁴, Paz Beniamini ^{1,8,15}, Christian Aa. Diget ¹³, Dmitry Frederiks ⁵, John Goldsten ¹², Adam Goldstein ⁶, Alexander D. Hall-Smith ¹³, Erin Kara ⁹, Alison M. Laird ¹³, Gavin P. Lamb ¹⁶, Oliver J. Roberts ⁶, Ryan Seeb ^{17,18}, V. Ashley Villar ^{19,20}, Aldana Holzmann Airasca ^{19,21,22}, Joseph R. Barber ²³, P. Narayana Bhat ²⁴, Elisabetta Bissaldi ^{21,25}, Michael S. Briggs ^{24,26}, William H Cleveland ⁶, Sarah Dalessi ^{24,26}, Davide Depalo ^{21,25}, Misty M. Giles ²³, Jonathan Granot ^{1,8,15}, Boyan A. Hristov ²⁴, C. Michelle Hui ¹⁷, Andreas von Kienlin ²⁷, Carolyn Kierans ², Daniel Kocevski ¹⁷, Stephen Lesage ^{24,26}, Alexandra L. Lysenko ⁵, Bagrat Mailyan ²⁸, Christian Malacaria ²⁹, Oindabi Mukherjee ⁶, Tyler Parsotan ², Anna Ridnaia ⁵, Samuele Ronchini ^{10,11,30}, Lorenzo Scotton ²⁴, Aaron C. Trigg ³¹, Anastasia Tsvetkova ^{5,32}, Mikhail Ulanov ⁵, Péter Veres ^{24,26}, Maia Williams ^{33,34}, Colleen A. Wilson-Hodge ¹⁷ and Joshua Wood ¹⁷

Affiliations are listed at the end of the paper

Accepted 2025 November 12. Received 2025 November 10; in original form 2025 September 26

ABSTRACT

Gamma-ray bursts are the most luminous electromagnetic events in the Universe. Their prompt gamma-ray emission has typical durations between a fraction of a second and several minutes. A rare subset of these events have durations in excess of a thousand seconds, referred to as ultra-long gamma-ray bursts. Here, we report the discovery of the longest gamma-ray burst ever seen with a $\sim 25\,000$ s gamma-ray duration, GRB 250702B, and characterize this event using data from four instruments in the InterPlanetary Network and the Monitor of All-sky X-ray Image. We find a hard spectrum, subsecond variability, and high total energy, which are only known to arise from ultrarelativistic jets powered by a rapidly spinning stellar-mass central engine. These properties and the extreme duration are together incompatible with all confirmed gamma-ray burst progenitors and nearly all models in the literature. This burst is naturally explained with the helium merger model, where a field binary ends when a black hole falls into a stripped star and proceeds to consume and explode it from within. Under this paradigm, GRB 250702B adds to the growing evidence that helium stars expand and that some ultra-long GRBs have similar evolutionary pathways as collapsars, stellar-mass gravitational wave sources, and potentially rare types of supernovae.

Key words: methods: observational – gamma-ray burst: individual: GRB 250702B – gamma-rays: general.

1 INTRODUCTION

Gamma-ray bursts (GRBs) are brief flashes of gamma-rays that are traditionally separated into classes based on their prompt duration, referred to as short and long GRBs separated by a fiducial 2 s threshold. Using ‘GRB’ as a phenomenological term, the shortest class of GRBs are magnetar giant flares (E. P. Mazets et al. 2008; E. Burns et al. 2021; J. Rastinejad et al. 2021; A. C. Trigg et al. 2025).

However, the majority of short GRBs arise from neutron star mergers, as confirmed with associated kilonovae and gravitational waves (S. I. Blinnikov et al. 1984; B. Paczynski 1986; D. Eichler et al. 1989; B. P. Abbott et al. 2017). Most long GRBs arise from collapsing rapidly rotating massive stars known as collapsars, as verified with associations to broad-line type Ic supernovae (T. J. Galama et al. 1998; A. I. MacFadyen & S. E. Woosley 1999; Z. Cano et al. 2017). Neutron star merger and collapsar GRBs are powered by collimated ultrarelativistic outflows called jets. In these progenitor cases, the prompt emission is followed by broad-band synchrotron radiation observed across the electromagnetic spectrum, which is referred to as afterglow. Lastly, a small number of GRBs have later been identified

* E-mail: eliza.neights@gmail.com (EN); ericburns@lsu.edu (EB)

† These authors contributed equally to this work.

Table 1. The instruments utilized for each analysis. Primary instruments are those that are used in the reported values. Secondary instruments provide confirmation.

	<i>Fermi</i> -GBM	Konus-Wind	<i>Psyche</i> -GRNS	<i>Swift</i> -BAT	MAXI
Duration	–	Primary	Primary	Primary	Primary
Minimum variability time-scale	Primary	–	–	Secondary	–
Maximum photon energy	Primary	–	Secondary	–	–
Spectra	Primary	Primary	–	–	–
Quasiperiodic oscillations	–	Primary	–	–	–

to originate from the tidal disruption of stars by supermassive black holes at the centre of galaxies, with prompt durations of a few days (J. S. Bloom et al. 2011; S. B. Cenko et al. 2012; G. C. Brown et al. 2015).

Ultra-long GRBs are a rare class with prompt durations of $\gtrsim 1000$ s (R. W. Klebesadel, J. G. Laros & E. E. Fenimore 1984; V. Connaughton 1998a, b; Y. Y. Tikhomirova & B. E. Stern 2005; A. J. Levan et al. 2014). When excluding tidal disruption events (TDEs), the longest gamma-ray duration of such an event is $\sim 15\,000$ s for GRB 111209A (S. Golenetskii et al. 2011; P. Vreeswijk, J. Fynbo & A. Melandri 2011). This event was associated with SN 2011kl, the most luminous supernova seen following a GRB (G. Stratta et al. 2013; M. C. Bersten et al. 2016; D. A. Kann et al. 2019). GRB 101225A, another ultra-long GRB with prompt duration $\gtrsim 2000$ s, also has some evidence for supernova emission (C. C. Thöne et al. 2011). Theoretically, the longest accretion time possible with a collapsar GRB is a few thousand seconds, physically limited by the angular momentum in a star spinning at break-up velocity (see fig. 7 of C. L. Fryer et al. 2025, in which break-up velocity is achieved in the tight binary scenario, but the limit is general). As we generally expect the prompt emission time-scale to be of similar order to the accretion time, collapsars struggle to explain the longest ultra-long GRBs.

GRB 250702B was first identified when the *Fermi* Gamma-ray Burst Monitor (*Fermi*-GBM) triggered multiple times over a ~ 3 h period on 2025 July 2 in response to impulsive signals consistent with originating from the same position (E. Neights et al. 2025a, b). The prompt emission of GRB 250702B was observed by numerous X-ray and gamma-ray monitors (J. DeLaunay et al. 2025; D. Frederiks et al. 2025; Y. Kawakubo et al. 2025; SVOM/GRM Team 2025), with Konus-Wind identifying the duration of this event as at least comparable to GRB 111209A. The *Einstein Probe* (EP) Wide-field X-ray Telescope observed X-rays from GRB 250702B in individual exposures over a 17 h period on July 2, and a stacking analysis found a signal beginning a day earlier on July 1 (H. Q. Cheng et al. 2025). The first precise localization of GRB 250702B is (RA, Dec) = $(284.6901^\circ, -7.8741^\circ)$ with an uncertainty of 2 arcsec, measured by the *Swift* X-Ray Telescope (*Swift*-XRT J. A. Kennea et al. 2025), which is the position used for our analysis.

Follow-up observations were performed across the electromagnetic spectrum, with detections in near-infrared, X-ray, and radio (K. D. Alexander et al. 2025; P. Atri et al. 2025; A. J. Bright, F. Carotenuto & P. G. Jonker 2025; N. Grollimund et al. 2025; A. J. Levan et al. 2025b, c; A. Martin-Carrillo et al. 2025; B. O'Connor et al. 2025; A. I. Sfaradi et al. 2025), and non-detections in optical and very high-energy gamma-rays (R. L. Becerra et al. 2025; M. Busmann et al. 2025; M. de Naurois 2025; A. Kumar et al. 2025; X. Li et al. 2025b; D. Paneque et al. 2025; I. Pérez-García et al. 2025; M. H. Siegel & *Swift*/UVOT Team 2025). Observations by the Very Large Telescope and *Hubble Space Telescope* resolved the host galaxy, proving an extragalactic origin of GRB 250702B and

showing the event as offset from the host galaxy centre, disfavouring a supermassive black hole TDE origin (A. J. Levan et al. 2025a). The multiwavelength follow-up observations can be modelled as synchrotron radiation from a fairly typical forward and reverse shock (J. D. et al. Carney et al. 2025; A. J. Levan et al. 2025a; B. O'Connor et al. 2025). B. P. et al. Gompertz et al. (2025) utilize data from the *James Webb Space Telescope* (*JWST*) to measure a redshift of 1.036, show the position of GRB 250702B to be in a star-forming region, and show no obvious transient at the position of GRB 250702B at 25.5 d after the GRB in the rest frame of the source.

Here, we present the gamma-ray analysis of GRB 250702B. The extreme duration and unusual properties of this event require combining observations from multiple monitors to gain a complete understanding. We describe our analysis in Section 2, and the physical inferences which follow in Section 3. In Section 4, we discuss the progenitor options that can be excluded based on the gamma-ray observations. The combination of the duration and rapid variability of GRB 250702B require an alternative origin, which we propose in Section 5 is a helium star merger. All times in this work are referenced against mid-night UTC on July 2, 2025, i.e. $T_0 = 2025-07-02T00:00:00$. Throughout this paper, we use the final cosmological parameters measured from the *Planck* mission (Planck Collaboration VI 2020): $H_0 = 67.4 \text{ km s}^{-1} \text{ Mpc}^{-1}$ and $\Omega_m = 0.315$ for a flat universe.

2 PROMPT GAMMA-RAY BURST ANALYSIS

GRB 250702B was detected by several GRB monitors, five of which are used in this paper: *Fermi*-GBM (C. Meegan et al. 2009), Konus-Wind (R. L. Aptekar et al. 1995), the Burst Alert Telescope onboard the *Neil Gehrels Swift Observatory* (*Swift*-BAT; S. D. Barthelmy et al. 2005), the *Psyche* Gamma-Ray and Neutron Spectrometer (*Psyche*-GRNS; D. J. Lawrence et al. 2025), and the Monitor of All-sky X-ray Image (MAXI) (M. Matsuoka et al. 2009). Individually, each instrument only contributes partial information necessary to fully characterize this event. As such, we use the appropriate instruments for each analysis, measuring each quantity with more than one instrument when possible as summarized in Table 1.

Fermi-GBM is in low Earth orbit and therefore has only partial coverage of GRB 250702B due to Earth occluding the source and detector downtime as a result of orbital regions of high particle activity. *Fermi*-GBM provides photon-by-photon continuous data with high spectral and precise temporal resolution across the 8 keV to 40 MeV band using two Bismuth Germanate (BGO) detectors and twelve Sodium Iodide (NaI) detectors (C. Meegan et al. 2009). However, its background stability is on the order of a minute.

Swift-BAT is also in low Earth orbit with partial sky coverage. It is a coded aperture mask allowing for arcminute level spatial information. It has an instantaneous field of view of ~ 15 per cent of the sky and serendipitously observes ~ 80 per cent of the sky each

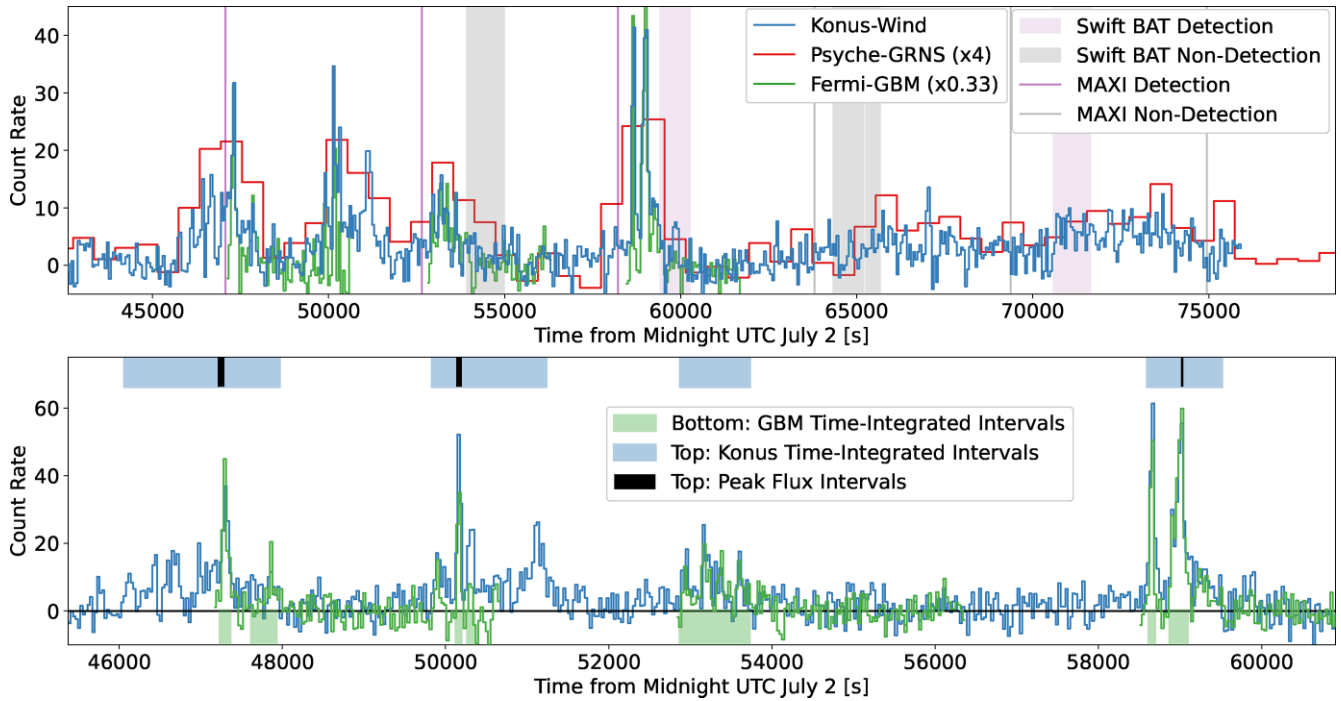


Figure 1. The combined background-subtracted gamma-ray light curve of GRB 250702B. For *Konus-Wind*, we show counts in the 75–315 keV energy range, for *Psyche-GRNS* the 30–230 keV energy range, and for *Fermi-GBM* 50–500 keV for NaI and 400–2000 keV for BGO detectors. Detector light curves are scaled and *Psyche* is shifted by 1000 s (to account for light travel time) for visualization. Intervals where the data for a given instrument are not useful are removed (i.e. times with unrelated GRBs, Earth-occulted times, etc.). *Top*: light curves for *Psyche-GRNS* with 600 s temporal resolution and *Konus-Wind* and *Fermi-GBM* both at 120 s temporal resolution. The prompt gamma-ray emission from GRB 250702B begins at least by $T_0 + 46\,074$ s based on the rapid rise and lasts at least until $T_0 + 71\,600$ s based on the last significant flare, as confirmed by *Swift*-BAT emission from the source. The BAT non-detections show the burst has quiescent intervals. MAXI information confirms these results. *Bottom*: a view of the brightest region of gamma-ray emission with *Fermi-GBM* and *Konus-Wind* data shown at 30 s resolution. Also shown are the selection intervals for detailed analyses.

day. *Swift* points at fixed positions, allowing for characterization of signals on long time-scales. The detectors are composed of Cadmium Zinc Telluride, which measure energies in the ~ 15 –350 keV range (S. D. Barthelmy et al. 2005).

Konus-Wind is far from Earth and thus has total coverage of the event. It is a transient monitor in a Lissajous orbit around the first Lagrange point of the Sun–Earth system at a distance of ~ 5 light seconds. *Konus-Wind* consists of two identical thallium-doped NaI spectrometers S1 and S2, pointing to the ecliptic poles. As it did not trigger on GRB 250702B, we utilize the continuous (waiting mode) data, which has 2.944 s temporal resolution. We use the S2 detector for most analyses, in which GRB 250702B is at an incident angle of 75.2° , which has three energy bands: 18–76, 76–316, and 316–1250 keV. We also use the S1 detector in one analysis, with energy bands 23–96, 96–398, and 398–1628 keV.

The *Psyche-GRNS*, also far from Earth with full coverage of the event, contains a Germanium detector built to determine the composition of the asteroid 16 Psyche. The GRNS is surrounded on most sides by a plastic scintillator anticoincidence shield built to separate cosmic rays from photons. It is this anticoincidence shield which we use as a GRB instrument within the InterPlanetary Network, which will be detailed in a future publication. These data have the most stable backgrounds and complete coverage, but the temporal resolution for continuous data is 600 s and the photon response has not yet been calculated. Light curves of GRB 250702B use the low-energy channels covering ~ 30 –230 keV, while the maximum photon energy analysis uses the high-energy channels covering $\gtrsim 350$ keV.

The MAXI is an X-ray monitoring instrument mounted on the Japanese Experiment Module-Exposed Facility aboard the International Space Station. Operating since 2009, it conducts nearly continuous all-sky surveys in the 0.2–30 keV energy range using Gas Slit Cameras (GSC) and Solid-state Slit Cameras (SSC). MAXI scans most of the sky every 92 min, allowing for serendipitous coverage of the position of GRB 250702B.

2.1 Gamma-ray light curve and duration

We combine information from a number of instruments to build the light curve shown in Fig. 1 and determine the duration of GRB 250702B with the approach detailed in Appendix A. We find that the prompt gamma-ray duration begins by $T_0 + 46,074$ s from the onset of *Konus-Wind* emission and lasts at least until $T_0 + 71,600$ s from the end of the last *Swift*-BAT significant detection. This gives an observed gamma-ray duration of $\gtrsim 25\,000$ s and up to $\sim 30\,000$ s based on emission whose association is ambiguous. This corresponds to a rest-frame duration of $\gtrsim 12\,500$ s. For comparison, the previous record holder was GRB 111209A, measured by *Konus-Wind* to have a prompt duration of $\sim 15\,000$ s and a rest-frame duration of ~ 9000 s (S. Golenetskii et al. 2011; P. Vreeswijk et al. 2011). GRB 250702B is unambiguously the longest GRB ever identified, shown in Fig. 2.

Appendix A also shows a search for gamma-ray emission over wider intervals, identifying no confident detections. Because of the extended X-ray emission beginning on July 1, we calculate upper limits on the gamma-ray emission at these times. Using *Konus-Wind* data we calculate an approximate upper limit for a soft spectrum

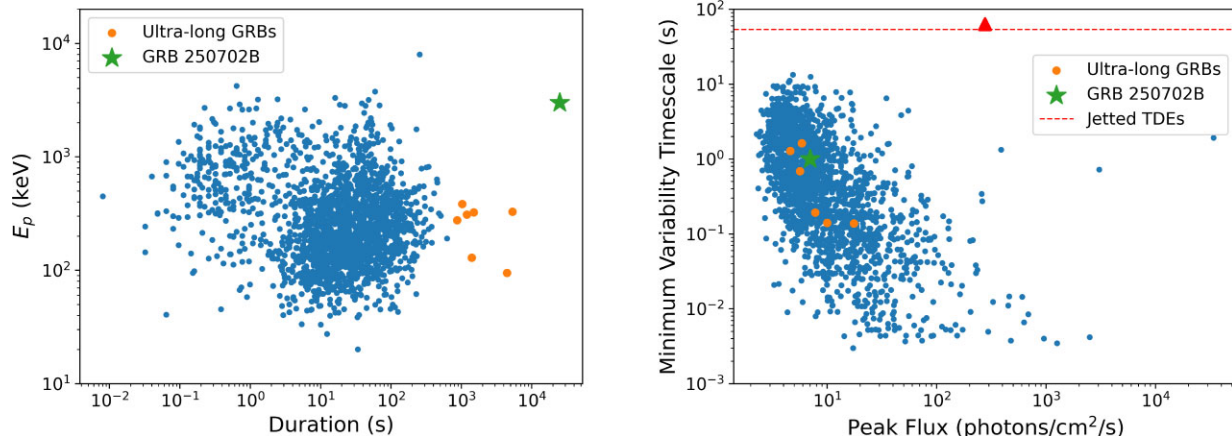


Figure 2. GRB 250702B in the context of *Fermi*-GBM GRBs. *Left*: the duration and peak energy in the peak flux interval. *Right*: the observed MVT as a function of 64 ms peak photon flux. Also shown is an approximate lower limit on the known MVT from TDEs, based on *Swift* J1644+57, detailed in Appendix C5. While the duration of GRB 250702B is an extreme outlier and the E_p is unusually high, the MVT and peak flux are typical values.

on the 2.944 s time-scale of $\sim 1.5 \times 10^{-7}$ erg cm $^{-2}$ s $^{-1}$. This is the deepest limit available from a mission with nearly complete coverage of the event.

2.2 Minimum variability time-scale

The minimum variability time-scale (MVT) is the shortest time-scale over which statistically significant variability is detected in the light curve. This is linked to the size and dynamics of the emitting region, with shorter MVTs suggesting a smaller emission region or faster central engine variability due to the finite speed of light. We compute the MVT following the procedure in V. Z. Golkhou & N. R. Butler (2014), in which a sliding wavelet is used to compare the measured variability power to that from random statistical fluctuations.

We analyse the *Fermi*-GBM triggers listed in Table A5 in Appendix A2.2 using 0.1 ms bins, as well as the bright GBM analysis intervals described in Table A6 and Table A7, and shown in Fig. 1, using 1 ms bins. In all cases, we use NaI detectors with a viewing angle within 60° of the source. The shortest MVT values arise from T0+47 285–47 300 s, T0+50 068–50 359 s, and T0 + 589 75–58 990 s, with values of 1.2 ± 0.5 s, 1.0 ± 0.4 s, and 1.4 ± 0.7 s, respectively. We perform a similar analysis using the *Swift*-BAT event data, available around the *Fermi*-GBM triggers via the Gamma-ray Urgent Archiver for Novel Opportunities (GUANO; A. Tohuvavohu et al. 2020) pipeline, finding weaker constraints (i.e. larger MVT). The figures showing these fits and the BAT table are shown in Appendix B1. As the MVT is an upper limit, and the signal-to-noise ratio (SNR) is low, these results are consistent. We therefore measure an MVT of ~ 1 s for GRB 250702B. This is well within the normal distribution for GRBs from stellar-mass central engines, as shown in Fig. 2. In the rest frame, the MVT is ~ 0.5 , giving subsecond variability.

2.3 Spectral lags

The temporal difference between the light curves of a GRB in different energy bands is known as spectral lag. The spectral lag is defined as positive when high-energy photons precede low-energy photons. In general, long GRBs show a positive spectral lag (L. X. Cheng et al. 1995; D. L. Band 1997; J. P. Norris, G. F. Marani & J. T. Bonnell 2000; T. N. Ukwatta et al. 2010), while short GRBs are

Table 2. Summary of significant spectral lag measurements, where the cross-correlation SNR exceeds the detection threshold of 3 and the fit is numerically stable. The measured spectral lag is consistent with zero for all intervals.

GBM interval	Bin width (s)	Spectral lag (s)	SNR
1a	0.256	0.02 ± 0.14	3.81
	0.512	-0.1 ± 0.4	3.25
2	0.256	0 ± 30	3.18
3a	0.064	0.4 ± 0.3	3.05
6	0.512	0.0 ± 0.3	3.1
7a	0.256	0.0 ± 0.2	3.83
7b	0.512	0.3 ± 0.6	3.0
7d	0.512	0.2 ± 0.4	3.09

characterized by a spectral lag consistent with zero (J. P. Norris et al. 2000; T. N. Ukwatta et al. 2010). Spectral lag may therefore help in categorizing GRBs (N. Gehrels et al. 2006; J. P. Norris & J. T. Bonnell 2006; B. Zhang et al. 2006), though the measured difference between short and long bursts may be due to photon statistics.

We measure the spectral lag between the 25–50 and 100–300 keV light curves using the cross-correlation method on the GBM analysis intervals in Table A6. We use the NaI detectors with a viewing angle within 60° of the source. To identify the characteristic time-scale of the correlation, we test four different temporal bin widths for each interval: 0.064, 0.128, 0.256, and 0.512 s. A statistically significant correlation, defined by a cross-correlation function SNR > 3 , was detected in several intervals. In all of these, the measured spectral lag is consistent with zero, with significant and reliable measurements summarized in Table 2.

2.4 Spectrum

We perform time-resolved spectral analysis of bright intervals and peak flux intervals in both *Fermi*-GBM and Konus-Wind. The details of the background and source selections are described in Appendix A. The specifics of the spectral analysis and complete results are detailed in Appendix B2. The best-fitting spectra are summarized in Table 3. The results for bright intervals with robust background estimates are included here, summarizing the measurements we consider to be reliable.

Table 3. The spectral results of *Fermi*-GBM and Konus-Wind. All intervals are best fit with a cut-off power law, where α is the photon index and E_p is the peak energy. The analysis intervals are shaded on the light curve in Fig. 1. The *Fermi*-GBM results are reported for the preferred spectral fits for analysis intervals selected using Bayesian blocks, as well as the peak flux measured over a 1 s period within Interval 7. The total fluence values reported are lower limits as the source intervals considered do not include all intervals in which emission is observed. GBM uncertainties are given at the 90 per cent confidence level, and fluence and flux are reported over the 1 keV to 10 MeV energy range. The Konus-Wind results are reported for four intervals with the total being the combined spectral fit over all intervals, as well as during peak flux intervals. Konus uncertainties are given at the 1σ confidence level, and fluence and flux are reported over the 10 keV to 10 MeV energy range.

Instrument	Interval	Time range–T0 (s)	α	E_p (MeV)	Fluence (erg cm $^{-2}$)
GBM	1	47 245–47 355	$-1.22^{+0.08}_{-0.08}$	$3.5^{+0.2}_{-2}$	$6.1^{+0.6}_{-0.5} \times 10^{-5}$
	6	58 625–58 685	$-1.14^{+0.06}_{-0.06}$	$3.4^{+0.9}_{-0.7}$	$7.2^{+0.3}_{-0.4} \times 10^{-5}$
	7	58 880–59 085	$-1.24^{+0.04}_{-0.04}$	$4.3^{+1}_{-0.8}$	$1.79^{+0.07}_{-0.07} \times 10^{-4}$
	Total				$> 3.1^{+0.1}_{-0.1} \times 10^{-4}$
Konus	1	46 075–47 959	$-1.1^{+0.5}_{-0.3}$	$0.8^{+1.3}_{-0.2}$	$1.3^{+0.7}_{-0.2} \times 10^{-4}$
	2	49 843–51 227	$-1.2^{+0.3}_{-0.2}$	$0.8^{+0.7}_{-0.2}$	$1.2^{+0.4}_{-0.2} \times 10^{-4}$
	3	52 884–53 720	$-1.3^{+0.5}_{-0.2}$	$1.2^{+9}_{-0.6}$	$7^{+6}_{-2} \times 10^{-5}$
	4	58 607–59 505	$-0.6^{+0.4}_{-0.3}$	$0.7^{+0.3}_{-0.2}$	$1.4^{+0.3}_{-0.2} \times 10^{-4}$
	Total		$-1.0^{+0.3}_{-0.2}$	$0.8^{+0.6}_{-0.2}$	$4.6^{+1.5}_{-0.7} \times 10^{-4}$

Instrument	Interval	Time range–T0 (s)	α	E_p (MeV)	Flux (erg cm $^{-2}$ s $^{-1}$)
GBM	7	59 024.082–59 025.106	$-1.01^{+0.13}_{-0.2}$	3^{+2}_{-2}	$2.8^{+0.3}_{-0.4} \times 10^{-6}$
Konus	1	47 284.533–47 308.085	$-0.8^{+0.5}_{-0.3}$	$0.8^{+1}_{-0.2}$	$7^{+4}_{-2} \times 10^{-7}$
	2	50 137.269–50 193.205	$-0.9^{+0.2}_{-0.2}$	$1^{+0.8}_{-0.3}$	$9^{+4}_{-2} \times 10^{-7}$
	4	59 019.316–59 034.036	$-0.7^{+0.4}_{-0.3}$	$0.8^{+0.6}_{-0.2}$	$8^{+3}_{-2} \times 10^{-7}$

Given the respective data limitations, the *Fermi*-GBM and Konus-Wind spectral results are in broad agreement. The indices generally agree, as do the fluence and peak flux values (once accounting for the different temporal selections and errors). All intervals are best fit with a cut-off power-law model with photon index between ~ -1.3 and ~ -0.6 . Both instruments report peak energy (E_p) values that are high for long GRBs, though the values disagree. Because we are limited to continuous data from Konus, the available energy channels preclude measuring E_p above ~ 1.5 MeV. GBM measures multiple intervals with $E_p \gtrsim 3$ MeV. As these values are measured with two background approaches and we find maximum photon energies of at least 5 MeV (Section 2.6), GRB 250702B has an unusually high peak energy for a long GRB (e.g. S. Poolakkil et al. 2021).

2.5 Intrinsic energetics

The observed peak flux and fluence at Earth can be converted into isotropic-equivalent total intrinsic peak luminosity, L_{iso} , and total energetics, E_{iso} , by accounting for the inverse-square law and converting to a rest-frame bolometric energy range, i.e. 1–10 000 keV, after accounting for cosmological expansion and redshift (J. S. Bloom, D. A. Frail & R. Sari 2001). The Konus time-integrated spectral fit gives $E_{\text{iso}} \gtrsim 1.4^{+0.4}_{-0.2} \times 10^{54}$ erg and rest-frame peak energy $E_{p,i,z} = 1.7^{+1.3}_{-0.4}$ MeV. Adding the sum of the GBM measurements and accounting for the partial coverage gives reasonably consistent results. Konus data gives $L_{\text{iso}} = 4.8^{+2}_{-1.0} \times 10^{51}$ erg s $^{-1}$ with a peak flux peak energy $E_{p,p,z} = 1.6^{+1.3}_{-0.4}$ MeV while GBM data gives $L_{\text{iso}} \sim 4.0 \times 10^{51}$ erg s $^{-1}$ and $E_{p,p,z} = 6^{+4}_{-4}$ MeV.

These measures allow us to place GRB 250702B in the context of other bursts, shown in Fig. 3, showing fairly typical E_{iso} and L_{iso} , but the ratio between these values is a clear outlier to the broader

distribution shown. The Amati and Yonetoku relations are shown in Fig. 4. Intriguingly, GRB 250702B is harder than expected from the broader long GRB Yonetoku relation, with the GBM E_p resulting in even greater inconsistency than the Konus value. Further, other ultra-long GRBs also exceed the expected E_p value for their luminosity at the $\gtrsim 90$ per cent level, suggesting a distinct population.

A. J. Levan et al. (2025a) and B. O’Connor et al. (2025) utilize afterglow measurements to infer properties of the jet, including the isotropic-equivalent kinetic energy, $E_{k,\text{iso}}$ and an exceptionally narrow half-jet opening angle, $\theta_j \lesssim 1^\circ$. B. O’Connor et al. (2025) find the collimation-corrected kinetic energy to be $E_{k,\text{coll}} = 3.5^{+1.4}_{-1.0} \times 10^{50}$ erg. With this, we infer a collimation-corrected gamma-ray energy release $E_{\gamma,\text{coll}} = 6^{+9}_{-6} \times 10^{49}$ erg. This together gives a total jet energy of $E_{\text{jet,coll}} = 4.1^{+1.6}_{-1.2} \times 10^{50}$ erg, and the gamma-ray efficiency is ~ 14 per cent $^{+20}_{-13}$ per cent. Using the Konus L_{iso} value, the collimation-corrected peak luminosity is $L_{\gamma,\text{coll}} = 2.0^{+3}_{-1.9} \times 10^{47}$ erg s $^{-1}$. These collimation corrected energetics are all within the normal distribution for typical long GRBs (A. Tsvetkova et al. 2017; B. O’Connor et al. 2023, 2025; A. J. Levan et al. 2025a). However, GRB 250702B has a higher E_p for its $E_{\gamma,\text{coll}}$ value compared to expectations from the broader population, while its peak luminosity L_p for its $L_{\gamma,\text{coll}}$ falls within the normal range (see fig. 13 A. Tsvetkova et al. 2021). This is the reverse of the isotropic-equivalent relations.

2.6 Maximum photon energy

Photons in excess of 1 MeV are often detected in GRB prompt emission and are used to put limits on the bulk Lorentz factor from pair opacity arguments. Thus, we seek to understand the highest energy photons observed from GRB 250702B. To quantify this, we

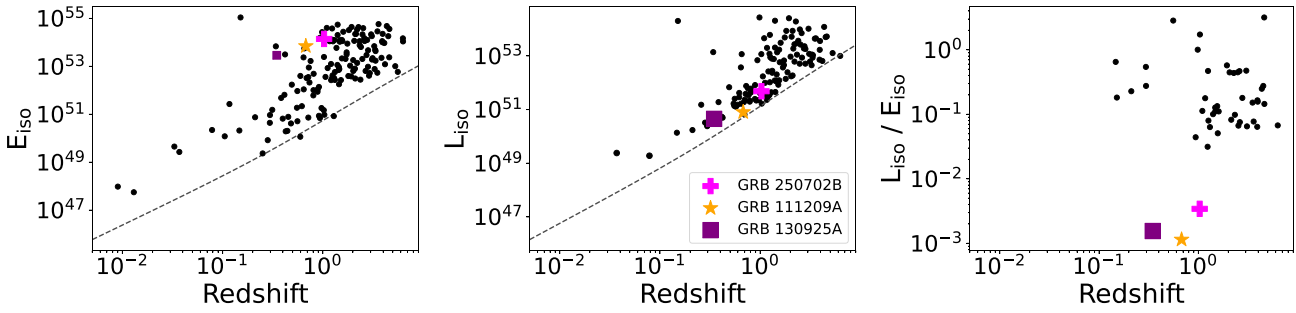


Figure 3. GRB 250702B intrinsic energetics compared to the broader population of GRBs from E. Burns et al. (2023). We also highlight the second and third longest bursts. These events have high E_{iso} and low L_{iso} values that fall within the known distributions, but have extreme ratios of these two values incompatible with the broader population. The dashed line in the left two plots correspond to the approximate *Fermi*-GBM detection threshold.

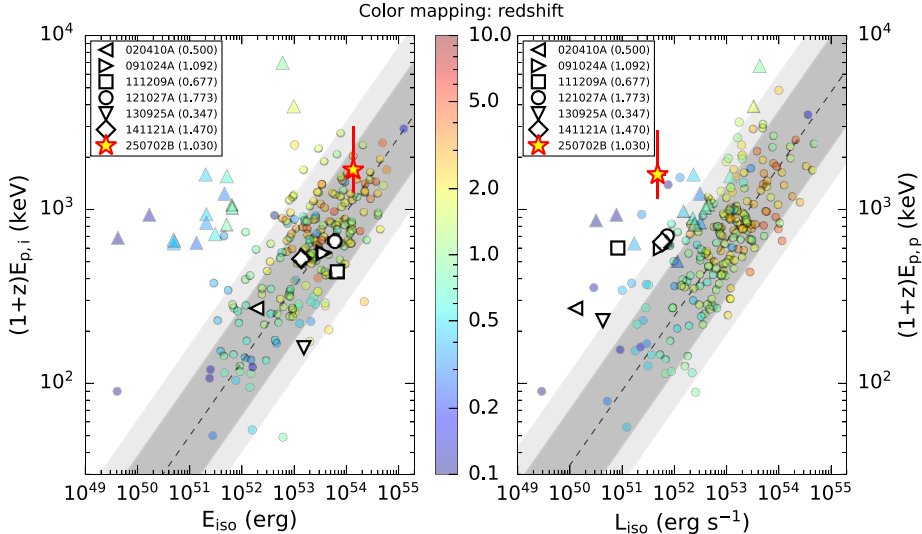


Figure 4. The Konus-Wind Amati (left) and Yonetoku (right) relations with 68 per cent and 90 per cent confidence intervals, using data from A. Tsvetkova et al. (2017, 2021). $E_{p,i}$ is the peak energy from the time-integrated interval, while $E_{p,p}$ is the peak energy from the peak flux interval. GRB 250702B is marked with a star, while other ultra-long GRBs (defined as durations above 1000 s) with measured redshift are shown with white shapes.

search *Psyche*-GRNS and *Fermi*-GBM data for the highest energy channel numbers which show significant emission using a basic SNR calculation. The *Psyche*-GRNS high-energy data channels 30–40 contain a 3σ excess from $T_0 + 58,100$ s to $T_0 + 59,400$ s (referenced to time at Earth), corresponding to a deposited energy of 2.1–2.8 MeV. In *Fermi*-GBM BGO data, analysis Interval 6 has a 3.4σ excess over 5.1–6.3 MeV and Interval 7 a 3.4σ excess over 4.9–5.5 MeV. The energy ranges here refer to the energy deposited into the detector which is a (probabilistic) lower bound on the incident photon energies. Thus, we have observer frame photons above $\gtrsim 5$ MeV, and rest-frame photons above $\gtrsim 10$ MeV.

2.7 Quasi-periodic oscillations

We use Konus-Wind data to search for quasi-periodic oscillations, taking advantage of the complete coverage of the $\sim 25\,000$ s gamma-ray emission interval and 2.944 s temporal resolution. We use two approaches, as detailed in Appendix B3. One method is a standard power spectrum analysis, leveraging the full photon statistics. The other is a cross-spectrum analysis, using both Konus detectors to isolate white noise and some instrumental effects. There is some excess at ~ 3 mHz but neither approach rejects the power-law only model at the 99 per cent confidence level (each reporting a p -value of

~ 2 per cent). Thus, we find no significant quasi-periodic oscillation in GRB 250702B, but we encourage similar searches in other ultra-long GRBs. We find no excess power at low frequencies, excluding the possibility raised in A. J. Levan et al. (2025a) of $\sim 2,825$ s periodicity.

3 PROMPT GAMMA-RAY BURST INFERENCES

The measurement of the gamma-ray properties in the previous section enable a number of key inferences on this event and the central engine which created it. These are crucial measurements for understanding the progenitor system. We briefly note the intrinsic energetics suggest a comparable total energy reservoir available to ultra-long GRBs compared to collapsars, with the only clear distinction being that this power dissipated over a far longer duration.

3.1 Central engine duration

The extreme observed duration requires a long-lived central engine. The 12,500 s rest-frame gamma-ray duration relates to the time-scale of the most rapid accretion (see Section 3.3). However, the central engine activity in GRB 250702B is longer than this time. First, early *Swift*-XRT observations beginning at $\sim T_0 + 92\,000$ s show

Table 4. Known or theoretical progenitors for GRB signatures, listed with their gamma-ray properties. The progenitor parameter values are only order of magnitude, reflecting significant theoretical or observational uncertainty, but are sufficient for our purposes. Viability is marked in the last column, sometimes relying on additional information detailed in the text, with the only viable options involving a stellar-mass compact object consuming a star and involving more angular momentum than can be contained within a star.

	Engine duration (s)	Minimum variability time-scale (s)	Maximum photon energy (MeV)	Power and profile	Viable (Y/N)
X-ray binaries	1000 000	–	0.5	Y	N
Magnetar giant flare	0.01–0.1	0.001–0.1	5	N	N
Neutron star mergers	0.01–10	0.001–1	10	N	N
White dwarf mergers	100–10 000	–	–	N	N
Tidal disruption event	250 000	$\gtrsim 40$	1	Y	N
IMBH tidal disruption event	$\sim 10 000$	$\gtrsim 10$	1	N	N
Micro tidal disruption event	10 000–100 000	0.01–10	10	Y	Y
Carbon–oxygen collapsar	1–1000	0.01–10	10	N	N
Helium collapsar	1–1000	0.01–10	10	N	N
Binary helium star merger	1–1000	0.01–10	10	N	N
Helium merger	$\sim 100 000$	0.01–10	10	Y	Y
GRB 250702B	$\sim 100 000$	0.5	10	–	–

rapid fading, indicative of the end of flaring behaviour (J. A. Kennea et al. 2025). Second, EP reports detections of this event beginning at T0-80 400 s from stacked observations (D. Y. Li et al. 2025a). At these distances, an X-ray signal must be produced by accretion and is a good indicator of central engine activity (T. Parsotan & D. Lazzati 2024). Therefore, the overall central engine time (rest-frame) is $\sim 85 000$ s. The bright and impulsive gamma-ray signal occurs $\sim 62 000$ –75 000 s in the rest-frame after the EP detection begins. This delay to peak power is unusual.

3.2 Bulk Lorentz factor

The coasting bulk Lorentz factor (Γ_0) of the relativistic jet, before it is decelerated by its interaction with the external medium, can be obtained from compactness arguments (T. Piran 1999). Since GRBs are intense sources of gamma-rays, an ultra-relativistic jet ($\Gamma_0 \gg 1$) is required so that the photons near and above the νF_ν peak energy, E_p , are not absorbed due to $\gamma\gamma$ -annihilation ($\gamma\gamma \rightarrow e^-e^+$). In this case, the spectral cut-off due to $\gamma\gamma$ -annihilation occurs at the energy $E_{\text{cut}} > E_p$ where the optical depth to $\gamma\gamma$ -annihilation is $\tau_{\gamma\gamma}(\Gamma_0, E_{\text{cut}}) = 1$. Here we model $\tau_{\gamma\gamma}(\Gamma_0, E)$ using the standard approach from J. Granot, J. Cohen-Tanugi & E. d. C. e. Silva (2008) to infer Γ_0 when a spectral cut-off is seen or obtain an estimate of the minimum Lorentz factor ($\Gamma_{0,\text{min}}$) when the observed spectrum only extends to some maximum energy (E_{max}). More details are provided in Appendix B4.

For GBM Interval 7 of GRB 250702B, the MVT is ~ 1.4 s and the maximum observed photon energy is $E_{\text{max}} \sim 5$ MeV, with both parameters listed in the observer frame. The best-fitting cut-off power-law model shows a spectral peak at $E_p \sim 4$ MeV, with a hard photon index $\alpha = -1.24$ below this energy. When interpreting the sharp spectral break as the high-energy spectral cut-off, with $E_{\text{cut}} = E_p$, this model yields an estimate of the true bulk Lorentz factor of $\Gamma_0 \simeq 81$ for the source redshift of 1.036. A power-law spectral model that also yields an acceptable fit to the data and extends to E_{max} is used to obtain $\Gamma_{0,\text{min}} = 56$. Both estimates compare favourably with Γ_0 inferences from afterglow studies (see Appendix B4 as well as A. J. Levan et al. 2025a and B. O’Connor et al. 2025) that also require an ultra-relativistic jet in this event. In both spectral models, we find that the emission region is highly optically thick to Thomson scattering by the created e^\pm -pairs, in which case the observed spectrum is significantly modified and explains the hard

photon index of $\alpha \gtrsim -2$ at energies below the spectral cut-off energy (R. Gill & J. Granot 2018).

3.3 Black hole size

The shortest variation which can be produced by an emitting region is determined by its physical size and the finite speed of light, i.e. a one light-second diameter object will not have variability at subsecond time-scales, though it can be longer. Thus, MVTs in emission from accretion discs give insight into the physical size of the central engine. In the case of black holes, the Schwarzschild crossing time-scales linearly with black hole mass, so constraints on physical size are also constraints on mass.

However, as detailed in Section 3.2, our analysis requires the emitting region to be moving towards us at relativistic velocities. The emission from relativistic jets typically occurs at a radius much larger than that of the central object. For example, a shell with a large Lorentz factor emitted with an interval Δt after an initial shell with a smaller Lorentz factor Γ collides with the latter at $R \approx 2c\Gamma^2\Delta t$. The Doppler contraction of the observed pulses means that the observed variability is much shorter than R/c and is instead of order $R/(2c\Gamma^2) \sim \Delta t$ (S. Kobayashi, T. Piran & R. Sari 1997). In other words, the two factors cancel out and the observed variability is on the order of the variability that is produced by the central engine. In practice, the observed values are substantially above this lower limit.

For example, for a stellar-mass black hole, this time-scale is $< 100 \mu\text{s}$, whereas the variability time-scales observed in GRB light curves, which are thought to host such stellar-mass black hole central engines, are orders of magnitude larger with typical values being ~ 0.01 –10 s (V. Z. Golkhou & N. R. Butler 2014). The gamma-ray emission from GRB 250702B has a rest-frame MVT of ~ 0.5 s and is produced in a relativistic jet. Based on the comparable MVTs seen in collapsar GRBs, which arise from $\sim 3 M_\odot$ black holes, we favour a stellar-mass central engine for GRB 250702B.

4 EXCLUDED PROGENITORS

A key question is the physical progenitor system which created this transient. We here describe numerous options from the literature which are sufficiently advanced to be testable, largely selected from C. L. Fryer et al. (2019) and from models invoked to explain previous ultra-long GRBs. Each model is compared with our results directly

as summarized in Table 4. A detailed discussion of each individual progenitor scenario, including scenarios where a normal collapsar produces such a long signal due to effects induced in propagation, is provided in Appendix C. We utilize the engine duration, power, and evolution discussion in Section 5 in our consideration of whether a given model can explain GRB 250702B.

Most long GRBs arise from collapsars, which are an ideal scenario to describe GRB 250702B except for the extreme duration. As detailed in the Section 5, extreme angular momentum can arrest material in the disc, extending accretion time. C. L. Fryer et al. (2025) explore the maximal durations that can occur when a star is spinning at breakup, where faster velocities would spin the star apart, finding a maximum value of a few thousand seconds. Thus, these events are inconsistent with the measured duration of GRB 250702B at two orders of magnitude, and we are motivated to explore other scenarios.

X-ray binaries and other Galactic sources are excluded by our ~ 10 MeV rest-frame photons and the identification of the host galaxy in A. J. Levan et al. (2025a). Magnetar giant flares and neutron star mergers are excluded because of insufficient durations by orders of magnitude. White dwarf mergers, carbon–oxygen collapsars, helium collapsars, and binary helium star mergers are excluded because their durations cannot reproduce the total central engine time by \sim two orders of magnitude and because each would predict a peak power at early times, in contrast to the significant delay to peak power observed in GRB 250702B.

Traditional TDEs from supermassive black hole mergers are excluded because of their long MVTs. For a direct comparison we repeat our MVT analysis for the *Swift*-BAT observation of the TDE *Swift* J1644+57 and find a rest-frame value of ~ 40 s (shown in Fig. 2 and detailed in Appendix C5). As this is the shortest MVT ever seen from a TDE, the MVT of known TDEs are $\gtrsim 2$ orders of magnitude greater than GRB 250702B. Follow-up observations also disfavour this origin due to the non-nuclear position of the transient with respect to the host and lack of late-time transient light (B. P. et al. 2025; A. J. Levan et al. 2025a)

A. J. Levan et al. (2025a), R. A. Eyles-Ferris et al. (2025), and D. Y. Li et al. (2025a) consider the possibility of a white dwarf tidal disruption by an intermediate-mass black hole (IMBH) to explain GRB 250702B. This model faces several issues. With respect to gamma-rays, such a model is still inconsistent with our MVT, as every cosmological event with subsecond variability seen previously is thought to have arisen from a stellar-mass black hole. Indeed, a white dwarf disrupting around an IMBH was already invoked to explain ~ 100 s variability (J. H. Krolik & T. Piran 2011) which is > 100 times larger than our value. Further, the duration of a white dwarf merger with an IMBH will not be longer than typical white dwarf mergers where the peak signal is ~ 150 s and the longest duration is less than 15 000 s, supported both by our subsequent central engine modelling as well as hydrodynamical simulations in B. O’Connor et al. (2025).

More generally, GRB 250702B appears to have fairly typical collapsar jet energetics except it is extreme in having a high peak energy and particularly narrow jet (B. O’Connor et al. 2025). Powerful jets are only known to arise from rapidly spinning black holes, with collapsar GRB stellar-mass black holes spun up during accretion of the star and active galactic nuclei spun up by accretion over enormous time-scales. The power from a Blandford–Znajek jet is proportional to both the accretion rate and the square of the black hole spin (equation 3); most engine models have similar relations. There is no obvious reason for an IMBH to be rapidly spinning in the prograde direction to the orbit of a white dwarf it disrupts. Even if

this occurs, a white dwarf is a substantially smaller energy reservoir than available in collapsars, even before accounting for losses to thermonuclear explosions (S. Rosswog, E. Ramirez-Ruiz & W. R. Hix 2009). The accretion power from these systems will be lower than models invoking stellar-mass black holes.

Narrow jets are thought to be collimated by their central engine and surrounding material. As an IMBH engine should be less efficient than a typical collapsar, and also have less material in the polar regions, there is no obvious explanation for the narrow jet. One may ameliorate these problems and the required energy reservoir by invoking disruption of a massive star around an IMBH, but this would exacerbate the MVT problems (M. J. Rees 1988; J. H. Krolik & T. Piran 2011).

In either IMBH case, there is also no obvious explanation for the significant delay to peak power output. Additionally, follow-up observations show a temporal decay more typical of GRB afterglow rather than the fiducial $-5/3$ power-law decay expected in TDEs (A. J. Levan et al. 2025a; B. O’Connor et al. 2025). Thus, we do not consider this model viable as an IMBH TDE origin would require black hole mass to MVT scalings which differ from other GRBs, expect different durations, power profiles, and temporal decays, and is unlikely to produce the jet properties seen in GRB 250702B.

5 HELIUM STAR MERGERS

The only models which naturally explain GRB 250702B involve a rapidly spinning stellar-mass black hole and a total energy reservoir of similar order to collapsar GRBs, given our measured intrinsic energetics. Since the duration cannot be achieved with the angular momentum possible in a single star (or two), orbital angular momentum must be tapped. Further, the orbital angular momentum must be added as the engine is starting, so that the star does not fully spin itself apart before accretion can occur. Thus, viable progenitor scenarios require the infall of a black hole into a star, with variations including evolution of field binaries, dynamical capture, or a hybrid option. We briefly introduce these options here.

Massive stars go through a series of expansion phases that, in binary systems, can lead to a situation where the binary companion is immersed in the expanding stellar envelope. Expansion can occur during hydrogen burning, after hydrogen exhaustion, and after helium depletion. The loss of orbital angular momentum in this common envelope scenario (through friction from tidal forces or bow shocks) cause the binary orbit to shrink (N. Ivanova et al. 2013). The helium merger scenario covers cases where a compact object falls into the secondary star in the system after hydrogen exhaustion (C. L. Fryer et al. 1999; W. Zhang & C. L. Fryer 2001).

For a fraction of these common envelope scenarios, the orbit tightens so much in the hydrogen common envelope that it ultimately merges into the helium core of the star. The angular momentum lost from the orbit goes into the helium star and when the black hole reaches the centre of the core, this high angular momentum will cause the helium core to accrete through a disc. This disc can produce the magnetic fields required to drive jets and viscosity in the disc will drive strong winds. The jet and winds will together explode the star and produce a supernova, similarly to the supernova engine in collapsars.

Variants of this system exist. The compact object can be a neutron star instead of a black hole. Because the neutron star will accrete rapidly due to neutrino cooling (C. L. Fryer, W. Benz & M. Herant 1996), it will quickly collapse to a black hole. The system will also occur in more evolved cores, after helium or even carbon–oxygen depletion. Thus, the phrase helium star merger generically refers to

the merger of a compact object, which is or will become a black hole, with a stripped star (C. L. Fryer et al. 1999). Such a model has been invoked to explain previous ultra-long GRBs including GRB 101225A (C. C. Thöne et al. 2011). We note that a helium star merger will occur only in regions with active star formation, as is seen in GRB 250702B (B. P. et al. Gompertz et al. 2025).

A related possibility is tidal capture of a star by stellar-mass compact object due to dynamical interactions in a dense stellar environment. The compact object can begin as a neutron star or a black hole, but a neutron star would accrete into a black hole. This results in a micro-TDE (H. B. Perets et al. 2016). Alternatively, micro-TDEs may also arise in field binaries, where the natal-kick due to the collapse of one star sends it into an eccentric orbit that results in disruption of the companion on the newly formed compact object. P. Beniamini, H. B. Perets & J. Granot (2025) shows that the association with a stellar-mass compact object naturally explains the rapid gamma-ray variability, hard gamma-ray spectrum, and off-centre galactic location. At the same time, the fallback time naturally explains the very long duration. The rates of partial/repeating disruptions via this channel are comparable to those of full disruptions. The former can provide a natural explanation for the observed X-ray precursor.

Helium star mergers (i.e. the merger of a compact object with a stripped star) are expected to occur fairly often in the Universe when compared with other GRB progenitors, since there is reason to believe helium stars expand (e.g. E. Van den Heuvel & P. Eggleton 1976; T. Linden, F. Valsecchi & V. Kalogera 2012; C. L. Fryer et al. 2025). When helium star mergers do occur, the extreme angular momentum and stellar-mass engine should power a jet. Thus, we focus on the field binary helium merger model below with Section 5.1 and Section 5.2 focusing on our expectations for jetted and supernova emission in GRB 250702B, and Section 5.3 discussing population-level expectations.

5.1 Jets

We seek to understand the properties of the jets which can be produced in helium mergers. Estimating the duration of jets produced in these mergers requires a set of assumptions about accretion time-scale and the jet power. We assume that the rotational angular momentum in the star post-merger is set by the orbital angular momentum lost as the compact remnant inspirals. The angular momentum profile of the star post-merger, compared to the angular momentum profiles of tidally locked binaries (C. L. Fryer et al. 2019) and single stars with moderate dynamo models locking different burning layers, is shown in Fig. 5.

For general exploration of GRB accretion times, the accretion rate is set by the sum of the free-fall time and disc accretion time for these mergers. The free-fall time is given by

$$t_{\text{ff}} = \frac{\pi r^{3/2}}{2\sqrt{2GM}}, \quad (1)$$

where r is the position of the material, G is the gravitational constant and M is the enclosed mass. The corresponding time-scale for accretion through an α -disc is

$$t_{\text{disc}} = \frac{2\pi r_{\text{disc}}^{3/2}}{\alpha\sqrt{GM}} = \frac{2\pi j_{\text{rot}}^3}{\alpha G^2 M^2}, \quad (2)$$

where r_{disc} is the radius where the material hangs up in the disc set by the specific angular momentum, j_{rot} , and α is the effective viscosity assuming a standard α -disc model (N. I. Shakura & R. A. Sunyaev 1973). Fig. 6 shows the accretion time-scales for our single star,

tidally spun-up, and merger models. Typically, the free-fall time is rapid. If the angular momentum is not extremely high, the disc is compact (e.g. 100–1000 km) and the free-fall time can dominate the accretion time-scale. This will be true for most models. For helium star mergers the extreme angular momentum sets the accretion time-scale. The helium star merger accretion time-scale can be orders of magnitude higher than any collapsar case and is the only scenario which can explain GRB 250702B. Other models are insufficient by more than an order of magnitude.

The accretion time-scale is not necessarily the same as the time-scale of the jet. The dependence of the jet power on the black hole spin (a_{BH}) and accretion rate through the disc (\dot{M}_{disc}) is still being studied. Here we use the R. D. Blandford & R. L. Znajek (1977) formula to determine the possible available power:

$$P_{\text{jet}} = 3 \times 10^{51} a_{\text{BH}}^2 \frac{\dot{M}_{\text{disc}}}{0.1 M_{\odot} \text{ s}^{-1}} \text{ erg s}^{-1} \quad (3)$$

From our accretion time-scale as a function of enclosed mass, we estimate the evolution of the black hole spin and the power in the Blandford–Znajek jet, as shown in Fig. 7. The luminosity is sensitive to the stellar models. For example, the large drop in the power above 10^5 s is due to the density jump at the boundary between the carbon–oxygen and helium layers of the star.

The total energy deposited into the jet is distributed into the prompt electromagnetic release, the kinetic energy of the jet, and contributes to the explosion of the supernova. As no supernova is observed following GRB 250702B (B. P. et al. Gompertz et al. 2025) we cannot quantify the latter. Thus, the sum of our measured gamma-ray and kinetic energies in the jet are a lower limit on the total jet power, which can be compared with our theoretical expectations. However, we must also account for accretion-to-jet efficiencies, which are at most a few per cent (G. Morales-Rivera et al. 2025; Z.-F. Wu et al. 2025), giving our theoretical expectation on the order of 1 per cent of the Blandford–Znajek prediction.

Fig. 7 gives the peak accretion power as $\sim(0.3\text{--}1)\times 10^{49}$ erg s $^{-1}$ for our two examples, predicting an approximate jet power of $\sim(0.3\text{--}1)\times 10^{47}$ erg s $^{-1}$. Our measurement of the GRB 250702B collimation-corrected peak luminosity is $\sim 2 \times 10^{47}$ erg s $^{-1}$. These values thus compare favourably.

Similarly, the sum of the total measured gamma-ray and kinetic energies is $\sim(2\text{--}6)\times 10^{50}$ erg (B. O’Connor et al. 2025). The integrated energy available in the $32 M_{\odot}$ helium star merger model is 3×10^{53} erg, and for the $60 M_{\odot}$ it is 7×10^{53} erg, giving a scaled expectation of $\sim(3\text{--}7)\times 10^{51}$ erg. We measure $\sim 4 \times 10^{50}$ erg, giving favourable agreement when accounting for the energy required for the predicted supernova. As a sanity check, we note the total energy of our helium merger model is comparable to the expected total energy from collapsar models ($\sim(2\text{--}3)\times 10^{53}$ erg), which with our 1 per cent efficiency expectation recover the observed collapsar total jet energies (e.g. B. O’Connor et al. 2023).

We emphasize that our helium merger model also explains the delay from central engine onset to duration, while nearly all other progenitor scenarios do not. The power will increase over a few $\times 10^4$ s before reaching the peak output for a similar time-scale, and is then followed by a \sim monotonic decrease in accretion over the next \sim day. This matches the profile inferred from EP and gamma-ray observations described in Section 3.1.

5.2 Supernova

The other major observable from these events will be supernovae. The JWST observations of GRB 250702B find no transient at the

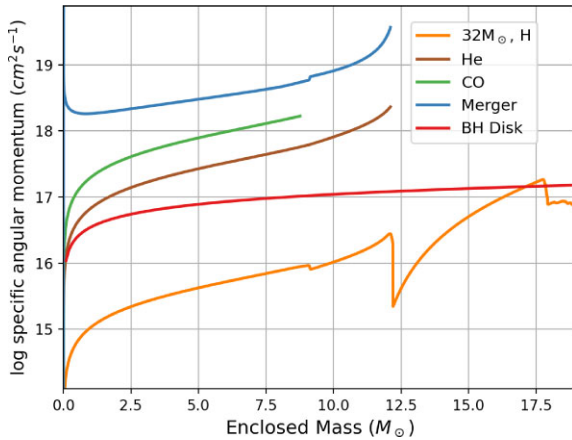


Figure 5. Specific angular momentum versus mass coordinate for a single hydrogen star with moderate dynamo models locking different burning layers, tidally locked helium and carbon–oxygen star collapsars (C. L. Fryer et al. 2019, 2025), and our helium star merger model. The two plots show the results for the cores produced by two different 1/10th solar metallicity stellar models ($32 M_{\odot}$ zero-age main sequence stars) at carbon–oxygen depletion. The required angular momentum to produce an accretion disc extending to 100 km for a black hole with a mass equal to the enclosed mass is included for comparison; a powerful jet requires an accretion disc at ~ 100 km, i.e. viable GRB models must exceed the black hole disk line above.

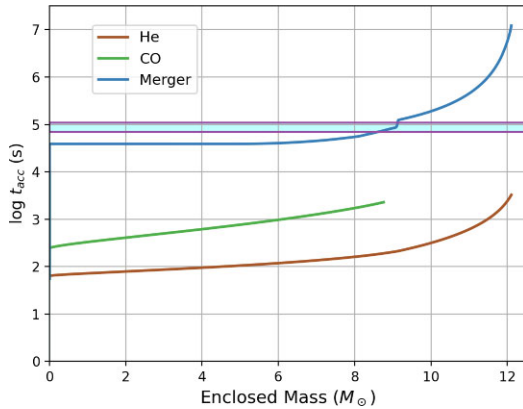
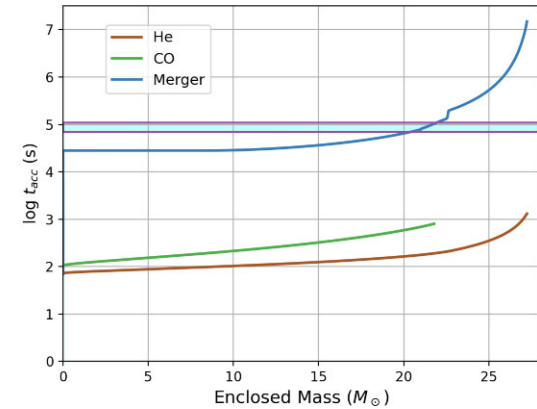
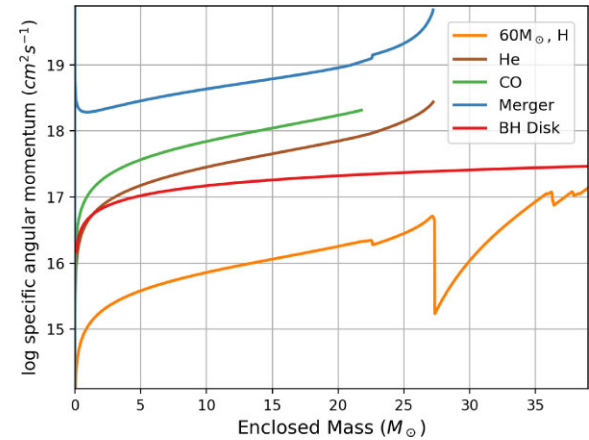


Figure 6. Accretion time-scales versus mass coordinate for the models in Fig. 5. The time-scales for single stars are dominated by the free-fall time, but the accretion time-scale for the helium merger is entirely set by the disc accretion time-scale. Our inferred central engine duration is shown as a horizontal line, where only the helium star merger is remotely viable.

position at a rest-frame time of $T_0 + 25.5$ d, excluding a typical Ic broad-lined supernovae seen following collapsar GRBs (B. P. et al. Gompertz et al. 2025). This does allow for less luminous supernovae to remain undetectable, due to the red galaxy and the high amounts of extinction. We thus seek to understand how a supernova following GRB 250702B may compare to those following classic collapsars.

Supernovae are generally powered at least partially by the heat from the radioactive decay of ^{56}Ni . Core-collapse supernovae are also powered by shock heating as the explosion front hits the circumstellar material. In collapsar GRBs it is the combination of the shock from the jet and the disc winds which explode the star at high velocities, with some ^{56}Ni created in the accretion disc which power the Ic-broad lined supernovae. We expect the same general picture in helium merger GRBs. However, supernovae following helium mergers could be any type of stripped-envelope supernova (as detailed below). We study these two power sources in the context of GRB 250702B.

^{56}Ni is expected to be produced in accretion discs, but the amount of ^{56}Ni production depends sensitively on the accretion rate and the black hole mass (which dictates the innermost radius of the disc). Fig. 8 shows the ^{56}Ni mass fraction as a function of the position in



the disc for a range of accretion rates. We assume that material is ejected across the entire disc (with perhaps some bias toward the inner region) as viscous heating drives a disc wind (for example, M. A. R. Kaltenborn et al. 2023). For the expected accretion rates and black hole masses in our helium merger scenario, we expect much of the material to be ejected from regions of the disc that do not produce ^{56}Ni , particularly for black hole masses above $5 M_{\odot}$. The ^{56}Ni yield from helium mergers will be much lower than typical collapsars. Assuming the maximal scenarios for ^{56}Ni in the models we consider, the highest yield would be only $\sim 0.075 M_{\odot}$. This is consistent with the *JWST* limit on a ^{56}Ni yield of $\lesssim 0.22 M_{\odot}$.

The lower accretion rates required to match the duration of GRB 250702B will produce weaker disc outflows. Further, in the case of a common envelope the region along the angular momentum axis could be relatively clean and the jet shock will deposit less power into the surrounding material. Thus, the stellar outflows will be weaker, and the shock heating in helium merger systems less powerful. All together, we expect the supernovae from these mergers to be much dimmer than typical collapsar models, being consistent with the *JWST* supernova non-detection (B. P. et al. Gompertz et al. 2025).

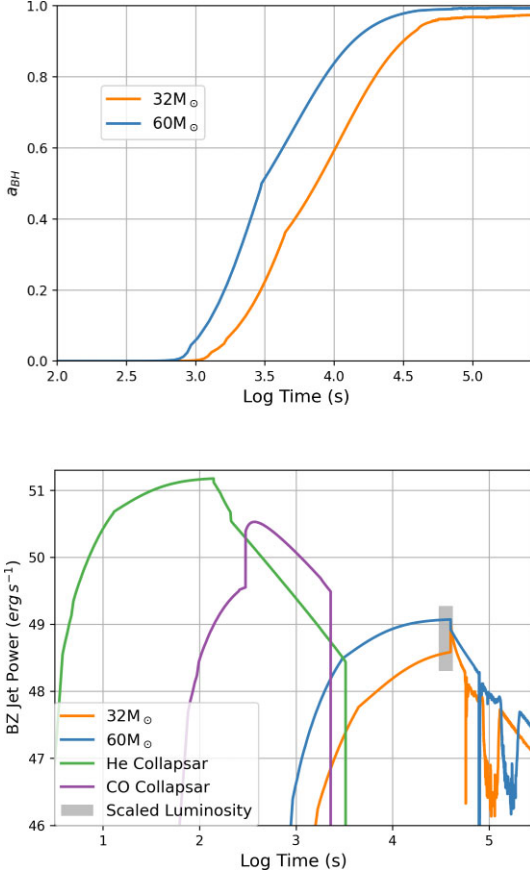


Figure 7. *Top:* the black hole spin as a function of time for our $32 M_{\odot}$ and $60 M_{\odot}$ helium star merger progenitors. For these calculations, we assume that the compact remnant spirals into the centre without accreting, with the compact remnant starting with a mass of $2 M_{\odot}$ and a spin ($\omega_{BH} = 0$). In reality, the compact remnant will accrete mass and spin up during the inspiral phase (W. Zhang & C. L. Fryer 2001). *Bottom:* the idealized Blandford-Znajek jet power from the combination of black hole spin and accretion rate in our systems of interest using equation 3. We include two tidally spun up collapsar models using the carbon–oxygen and helium cores of a $30 M_{\odot}$ zero-age main sequence star assuming they are in a tight binary with an orbital separation just beyond the Roche Radius (for more details, see C. L. Fryer et al. 2025). We overlay a representation of GRB 250702B, placing our peak gamma-ray duration at the peak from the helium merger models. We scale the $3 \times 10^{46} \text{ erg s}^{-1}$ time-averaged luminosity with efficiencies between 0.16 per cent for magnetically arrested discs to 1.5 per cent for Blandford-Znajek from Z.-F. Wu et al. (2025).

5.3 Population considerations

Population level expectations are key to exploring GRB progenitors. We here discuss whether past observations of GRBs and supernovae are consistent with our expectations of this model, and the population-level predictions which may be tested in future events.

We note the helium star merger model has been invoked in past events. While GRB 101225A has a duration which can be explained through other means, the faint supernova is consistent with the helium merger model expectation (C. C. Thöne et al. 2011). In contrast, GRB 111209A has the second longest duration but has the most luminous supernova seen following a GRB (D. A. Kann et al. 2019), possibly tied to the much wider jet half-opening angle of $\sim 20^\circ$ (G. Stratta et al. 2013) depositing more jet shock energy into the stellar envelope. Thus, if that is also a helium merger, the expected supernova brightness may have a large range of luminosities.

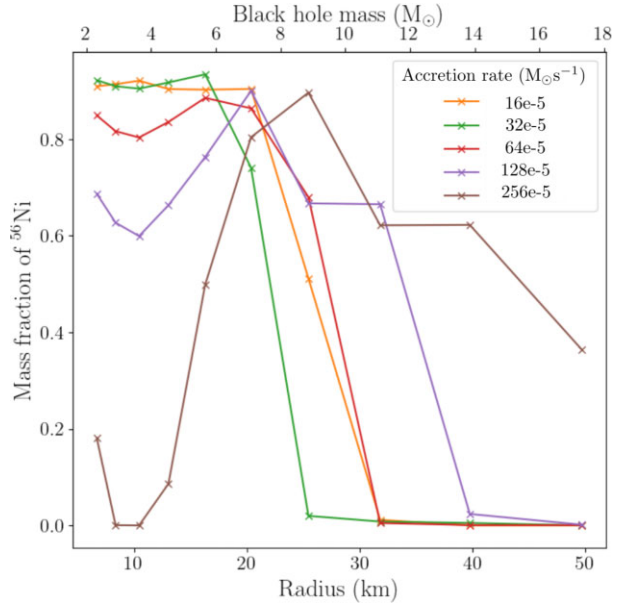


Figure 8. ^{56}Ni mass fraction as a function of the position in the accretion disc. The innermost radius depends upon the mass of the black hole. The innermost stable circular orbit for a maximally rotating black hole dictates the innermost radius of the disc. The upper x -axis shows the position of the innermost disc radius for a set of black hole masses at maximal spin. The ^{56}Ni in the disc drops precipitously when the black hole exceeds $5 M_{\odot}$ for all accretion rates expected for helium mergers. Lower mass black holes will produce some ^{56}Ni , but we expect the total yield to be low (S. E. D. Abrahams et al. 2023).

For GRB emission, the extreme angular momentum in helium mergers forces a long accretion time-scale, inconsistent with the duration of typical long GRBs. This explains the lack of Ib supernovae following typical long GRBs, though these may be observed in related transients (e.g. J. C. Rastinejad et al. 2025). The lower intrinsic luminosities of ultra-long GRBs limit detection distances, and the ultra-long durations make identification more difficult. Thus, we find no reason to disbelieve this progenitor channel from the archival GRB sample.

In the helium star merger scenario the associated supernova must arise from a stripped star. Thus, we may expect Ib and Ic supernovae. These may be broad-lined supernovae if enough energy is deposited into the stellar envelope (though supernova seem from these events off-axis may have lower observed velocities due to ejecta asymmetry). If significant hydrogen from the common envelope is swept up in the ejecta the associated supernova could be IIb. Similar physical models have been invoked to explain narrow emission-line supernovae. For example, B. D. Metzger (2022) suggest this progenitor for Ib and Icn supernovae, and, if so, could also explain (the currently unobserved) Idn, Ien (S. Schulze et al. 2025), and IIn supernovae (A. Gagliano et al. 2025). Here the supernovae is surrounded by circumstellar material which emits lines when heated by the supernova. This material would be ejected by the compact object interactions with the stripped star partner in the years before merging. These events do show lower ^{56}Ni yields than normal core-collapse supernovae (K. Maeda & T. J. Moriya 2022; D. Farias et al. 2025).

Additionally, if the merger is produced during a hydrogen common envelope event where the compact object continues to inspiral into the core of the star, we would expect an extensive circumstellar medium (with hydrogen). This would enhance the shock heating

and likely produce hydrogen features. The debris above the angular momentum axis for these hydrogen common envelope systems may contaminate the jet, preventing it from producing GRBs, producing supernovae (or fast blue optical transients) instead (B. D. Metzger 2022; H. Hamidani et al. 2025). Similarly, if the secondary star explodes before the black hole is engulfed, this matches the tight-binary scenario invoked to explain the angular momentum required for typical collapsar GRBs (C. L. Fryer et al. 2025), which relates to future stellar-mass gravitational wave sources.

Lastly, the host galaxy properties and offsets are key to probing other GRB progenitor channels. In the helium merger scenario, during the formation of the compact object, mass ejection and a potential compact remnant kick can cause the binary to gain a net momentum. The velocity distribution of these massive star binaries tends to peak at 20 km/s and extend, depending on the compact remnant kick up to 100–200 km/s. Only in these extreme cases would the merger occur far from the birthplace of these binary stars. As massive stars live only for a short time, the majority of helium mergers should occur close to where they are born. They will thus track active star formation in individual galaxies, occurring within the stellar field, and the cosmological star formation history as a population. Because the compact object can begin as a neutron star, these events should track host galaxies and metallicity dependencies more like standard core-collapse supernovae rather than the low metallicity preference of collapsars.

With future proof that this merger scenario occurs, we can start to gain insight into the merger process itself and the subsequent mass ejection. Coupled with radiation–hydrodynamics calculations of the shock interactions, we can use observations and observational limits of the associated supernova to probe both the properties of the explosion and the mass ejection during the last common envelope phase. Upper limits on the peak supernova emission place limits on the ^{56}Ni yield and shock heating. An observation, particularly with spectra determining the presence of hydrogen or helium lines, will provide crucial clues into the extent at which helium stars expand. This is already strongly suggested via GRB observations by this event and population-level inferences on collapsar GRBs (C. L. Fryer et al. 2025).

6 CONCLUSION

GRBs have been enigmatic objects since their discovery more than half a century ago. After detections of $\sim 15\,000$ GRBs, GRB 250702B is still unique. It has subsecond variability, typical intrinsic energetics, high bulk Lorentz factor, and no spectral lag, all of which are fairly typical in GRBs. However, it has record duration, is inconsistent with the peak energy for its luminosity in the collapsar Yonetoku relation (as are other ultra-long GRBs), and has an exceptionally narrow jet.

While we considered numerous GRB models, the only one which naturally explains the properties observed in GRB 250702B is the fall of a stellar-mass black hole into a star. We focus on the field binary evolution to a helium merger as our preferred explanation. This model makes a number of testable predictions, even with current knowledge. Ultra-long GRBs from helium mergers should track star formation, with individual events arising from star-forming regions and the population tracking the cosmic star formation rate evolution. They can arise from higher metallicity regions than collapsar GRBs. Lastly, helium merger GRBs should be followed by stripped-envelope supernovae.

There are a number of opportunities where theory and simulation investment are warranted. The unusual behaviour of an idealized

engine in the Blandford–Znajek scenario may allow for unique predictions and tests of accretion and jets. The types of stripped enveloped supernovae, such as broad-lined or narrow emission line supernovae, can likely be narrowed. Predictions on the minimal ^{56}Ni forged in accretion discs can be refined and form a floor for the minimal supernova luminosity. And modelling from long before merger may allow for constraints on amounts and distributions of viable circumstellar material.

Lastly, these events are difficult to identify. They are intrinsically lower luminosity than collapsar GRBs, which most instruments were designed to detect. The most sensitive GRB monitors are limited to low Earth orbit, where they lack the continuous viewing time-scales necessary to probe ultra-long GRBs. Certainly *Swift*, *Einstein Probe*, and *SVOM* provide opportunity to identify these events, but the broad characterization requires instruments like *Konus-Wind* and *Psyche-GRNS*. For the first time since the identification of ultra-long GRBs, we have two distant monitors with stable backgrounds on the required time-scales in these instruments, allowing for spatial information from the InterPlanetary Network. When paired with the new Legacy Survey of Space and Time by the Vera Rubin Observatory, we may expect more regular identification of ultra-long GRBs. Further, the *Compton Spectrometer and Imager* will be able to individually identify the brighter ultra-long events (J. Tomsick et al. 2024). Thus, we strongly encourage investment in theory, simulation, and prioritized follow-up of these events.

AUTHOR CONTRIBUTIONS

Eliza Neights helped with organizing the meetings and writing the paper, performed the complex *Fermi*-GBM background fitting and source selections used in her and other analyses, performed the *Fermi*-GBM spectral analysis and contributed related plots and text, and contributed general text to the paper. Eric Burns helped with organizing the meetings, bringing together the relevant teams, and the helium merger model scenario, contributed major text to all sections in the paper, performed the maximum photon energy analysis, calculated intrinsic energetics and placed the bursts in context, determined duration, performed the analysis of the high level *Psyche* data, and is co-lead of the InterPlanetary Network. Chris Fryer performed the quantitative work on the helium merger model, contributed key analysis on excluding other progenitor scenarios, and contributed much of the relevant text and figures. The KW team (Dmitry Svinkin, Dmitry Frederiks, Alexandra L. Lysenko, Anna Ridnaia, Anastasia Tsvetkova, and Mikhail Ulanov) performed the *Konus-Wind* analysis including the spectral analysis, the measures in intrinsic energetics, the Amati and Yonetoku relations and the analysis of the other ultra-long GRBs for their inclusion, the *Konus-Wind* gamma-ray upper limits over *Einstein Probe* intervals, the background fitting, and the relevant text. They also contributed to the interpretation of this and other data. Suman Bala contributed the MVT and spectral lag analyses. Rachel Hamburg performed the search for extended emission in *Fermi*-GBM. Ramandeep Gill provided the discussion on the required bulk Lorentz factor. Michela Negro contributed the cross-spectrum QPO analysis. Megan Master-son contributed the power-spectrum QPO analysis. Jimmy DeLaunay contributed the *Swift*-BAT analysis and relevant text and figures. David J. Lawrence processed the *Psyche*-GRNS data and provided instrument and mission expertise to enable proper handling of the data. Sophie E. D. Abrahams performed simulations leading to the ^{56}Ni production predictions. Yuta Kawakubo provided the MAXI detection and non-detection information. Paz Beniamini provided the text on tying minimum variability time-scale to central engine

size, key arguments excluding other progenitors, and contributed the text on the micro TDE scenario.

Christian Aa. Diget contributed to the ^{56}Ni production predictions. John Goldsten provided the channel to energy mappings for *Psyche*-GRNS to allow for proper data selection including the calculation of the maximum photon energy. Adam Goldstein provided input on the novel background approach and general use of the GDT. Alexander Hall-Smith contributed to the ^{56}Ni production predictions. Erin Kara provided expertise on the QPO analysis and viability of TDE progenitors. Alison Laird contributed to the ^{56}Ni production predictions. Gavin Lamb provided input on the viable and excluded models discussion. Oliver J. Roberts contributed to the maximum photon energy analysis and identified the third GBM trigger as arising from GRB 250702C. Ryan Seeb contributed to the GBM spectral analysis. V. Ashley Villar contributed to the discussions on the variety of viable supernovae and in particular the viability of ultra-long GRBs being related to type Ixn supernovae.

ACKNOWLEDGEMENTS

We thank B. P. et al. Gompertz et al. (2025), J. D. et al. Carney et al. (2025), and B. O'Connor et al. (2025) for the sharing of private data and analysis prior to the public release of their papers, enabling far greater conclusions in our work on a tight timeline. We additionally thank B. O'Connor for extremely helpful comments at an opportune time. We further thank E. Borowski for helpful information on X-ray binaries.

EN acknowledges NASA funding through Cooperative Agreement 80NSSC22K0982. OJR, AG, and SB graciously acknowledge NASA funding support from cooperative agreement 80NSSC24M0035. RS thanks the NASA OSTEM Internship program for providing support. PB's work was funded by a grant (no. 2020747) from the United States-Israel Binational Science Foundation (BSF), Jerusalem, Israel and by a grant (no. 1649/23) from the Israel Science Foundation. JD acknowledges support from NASA under award numbers NAS5-0136, 80NSSC25K7567, and 80NSSC25K7788. AML, CAD, ADH, and SEDA acknowledge support from the Science and Technology Facilities Council (STFC) through grants ST/V001035/1 and ST/Y000285/1. The work for JG, DL, and PP was funded by NASA's Discovery Program, under the Psyche: Journey to a Metal World mission. Psyche funding is provided to the Johns Hopkins University Applied Physics Laboratory (JHU/APL) through contract 1569206 from NASA Jet Propulsion Laboratory. The work of DSS, DDF, AVR, ALL, AET, and MVU was supported by the basic funding programme of the Ioffe Institute no. FFUG-2024-0002; AET also acknowledges financial support from ASI-INAF Accordo Attuativo HERMES Pathfinder operazioni n. 2022-25-HH.0. ACT's research was supported by an appointment to the NASA Postdoctoral Program at the NASA Marshall Space Flight Center, administered by Oak Ridge Associated Universities under contract with NASA. GPL acknowledges support from the Royal Society (grant nos. DHF-R1-221175 and DHF-ERE-221005).

DATA AVAILABILITY

The *Fermi* and *Swift* data underlying this article are available in the public domain on NASA HEASARC: <https://heasarc.gsfc.nasa.gov>. *Psyche*-GRNS data will be available on the Planetary Data System a few months after the event time. Konus-*Wind* and MAXI data can be requested from the respective instrument leads. Data and code generated for this project may be made available upon request to the lead author.

REFERENCES

Abbott B. P. et al., 2017, *ApJ*, 850, L40
 Abdo A. A. et al., 2009, *ApJ*, 707, 580
 Abrahams S. E. D., Fryer C., Hall-Smith A., Laird A., Diget C., 2023, in EPJ Web Conf., 279, 10002
 Ackermann M. et al., 2011, *ApJ*, 729, 114
 Alexander K. D. et al., 2025, GRB Coordinates Network, 41059, 1
 Alston W. N., Markeviciute J., Kara E., Fabian A. C., Middleton M., 2014, *MNRAS*, 445, L16
 Andreoni I. et al., 2022, *Nature*, 612, 430
 Aptekar R. L. et al., 1995, *Space Sci. Rev.*, 71, 265
 Arnaud K., Dorman B., Gordon C., 1999, Astrophysics Source Code Library, record ascl:9910.005
 Atri P., Rhodes L., Fender R., Hughes A., Motta S., XKAT Collaboration, 2025, GRB Coordinates Network, 41054, 1
 Ayal S., Livio M., Piran T., 2000, *ApJ*, 545, 772
 Band D. L., 1997, *ApJ*, 486, 928
 Band D. et al., 1993, *ApJ*, 413, 281
 Baring M. G., Harding A. K., 1997, *ApJ*, 491, 663
 Barthelmy S. D. et al., 2005, *Space Sci. Rev.*, 120, 143
 Becerra R. L. et al., 2025, GRB Coordinates Network, 40918, 1
 Beniamini P., Perets H. B., Granot J., 2025, preprint ([arXiv:2509.22779](https://arxiv.org/abs/2509.22779))
 Bersten M. C., Benvenuto O. G., Orellana M., Nomoto K., 2016, *ApJ*, 817, L8
 Blackburn L., Briggs M. S., Camp J., Christensen N., Connaughton V., Jenke P., Remillard R. A., Veitch J., 2015, *ApJS*, 217, 8
 Blandford R. D., Znajek R. L., 1977, *MNRAS*, 179, 433
 Blinnikov S. I., Novikov I. D., Perevodchikova T. V., Polnarev A. G., 1984, *Sov. Astron. Lett.*, 10, 177
 Bloom J. S., Frail D. A., Sari R., 2001, *AJ*, 121, 2879
 Bloom J. S. et al., 2011, *Science*, 333, 203
 Bright A. J., Carotenuto F., Jonker P. G., 2025, GRB Coordinates Network, 40985, 1
 Brown G. C., Levan A. J., Stanway E. R., Tanvir N. R., Cenko S. B., Berger E., Chornock R., Cucchiara A., 2015, *MNRAS*, 452, 4297
 Burns E. et al., 2021, *ApJ*, 907, L28
 Burns E. et al., 2023, *ApJ*, 946, L31
 Burns E., Veres P., Hui C. M., Fermi-GBM Team, 2024, GRB Coordinates Network, 36856, 1
 Burrows D. N. et al., 2011, *Nature*, 476, 421
 Busmann M., Hall X. J., O'Connor B., Gruen D., Sommer J., Palmese A., 2025, GRB Coordinates Network, 40949, 1
 Cano Z., Wang S.-Q., Dai Z.-G., Wu X.-F., 2017, *Adv. Astron.*, 2017, 8929054
 Carney J. D. et al., 2025, *ApJ*, 994, L46
 Cenko S. B. et al., 2012, *ApJ*, 753, 77
 Cheng L. X., Ma Y. Q., Cheng K. S., Lu T., Zhou Y. Y., 1995, *A&A*, 300, 746
 Cheng H. Q. et al., 2025, GRB Coordinates Network, 40906, 1
 Cheong P. C.-K., Pitik T., Longo Micchi L. F., Radice D., 2025, *ApJ*, 978, L38
 Chevalier R. A., 1989, *ApJ*, 346, 847
 Connaughton V., 1998a, in Paul J., Montmerle T., Aubourg E., eds, Abstracts of the 19th Texas Symposium on Relativistic Astrophysics and Cosmology. Paris, France, p. 13
 Connaughton V., 1998b, in Olinto A. V., Frieman J. A., Schramm D. N., eds, Eighteenth Texas Symposium on Relativistic Astrophysics. World Scientific, Chicago, US, p. 514
 de Niro M., 2025, GRB Coordinates Network, 41095, 1
 DeLaunay J., Ronchini S., Tohuvavohu A., Kennea J. A., Parsotan T., Williams M., 2025, GRB Coordinates Network, 40903, 1
 Eichler D., Livio M., Piran T., Schramm D. N., 1989, *Nature*, 340, 126
 Eyles-Ferris R. A. et al., 2025, preprint ([arXiv:2509.22843](https://arxiv.org/abs/2509.22843))
 Farias D. et al., 2025, preprint ([arXiv:2511.12362](https://arxiv.org/abs/2511.12362))
 Fitzpatrick G., Connaughton V., McBreen S., Tierney D., 2011, preprint ([arXiv:1111.3779](https://arxiv.org/abs/1111.3779))
 Frederiks D., Lysenko A., Ridnaia A., Svirkin D., Tsvetkova A., Ulanov M., Cline T., Konus-Wind Team, 2025, GRB Coordinates Network, 40914, 1
 Fruchter A. et al., 2006, *Nature*, 441, 463

Fryer C. L., Heger A., 2005, *ApJ*, 623, 302

Fryer C. L., Benz W., Herant M., 1996, *ApJ*, 460, 801

Fryer C. L., Woosley S. E., Herant M., Davies M. B., 1999, *ApJ*, 520, 650

Fryer C. L., Lloyd-Ronning N., Wollaeger R., Wiggins B., Miller J., Dolence J., Ryan B., Fields C. E., 2019, *Eur. Phys. J. A*, 55, 132

Fryer C. L., Burns E., Ho A. Y., Corsi A., Lien A. Y., Perley D. A., Vail J. L., Villar V. A., 2025, *ApJ*, 986, 185

Gagliano A. et al., 2025, *ApJ*, 989, 182

Galama T. J. et al., 1998, *Nature*, 395, 670

Gehrels N. et al., 2006, *Nature*, 444, 1044

Gendre B. et al., 2013, *ApJ*, 766, 30

Geppert U., Page D., Zannias T., 1999, *A&A*, 345, 847

Gierliński M., Middleton M., Ward M., Done C., 2008, *Nature*, 455, 369

Gill R., Granot J., 2018, *MNRAS*, 475, L1

Goldstein A., Burns E., Hamburg R., Connaughton V., Veres P., Briggs M. S., Hui C. M., The GBM-LIGO Collaboration, 2016, preprint (arXiv:1612.02395)

Goldstein A. et al., 2019, preprint (arXiv:1903.12597)

Goldstein A. et al., 2020, *ApJ*, 895, 40

Goldstein A., Cleveland W. H., Kocevski D., 2023, Fermi Gamma-Ray Data Tools: v2.0.0. Available at: <https://github.com/USRA-STI/gdt-fermi>

Golenetskii S. et al., 2011, GRB Coordinates Network, 12663, 1

Golkhou V. Z., Butler N. R., 2014, *ApJ*, 787, 90

Gompertz B., O'Brien P., Wynn G., 2014, *MNRAS*, 438, 240

Gompertz B. P. et al., 2023, *Nat. Astron.*, 7, 67

Gompertz B. P. et al., 2025, preprint (arXiv:2509.22778)

Granot J., Cohen-Tanugi J., Silva E. d. C. e., 2008, *ApJ*, 677, 92

Grollimund N., Corbel S., Coleiro A., Cangemi F., Rodriguez J., 2025, GRB Coordinates Network, 41147, 1

Guiriec S. et al., 2011, *ApJ*, 727, L33

Hamidani H., Ioka K., Kashiyama K., Tanaka M., 2025, *ApJ*, 988, 30

Hascoët R., Daigne F., Mochkovitch R., Vennin V., 2012, *MNRAS*, 421, 525

Ioka K., Hotokezaka K., Piran T., 2016, *ApJ*, 833, 110

Ivanova N. et al., 2013, *A&AR*, 21, 59

Jenke P. et al., 2016, *ApJ*, 826, 37

Kaltenborn M. A. R., Fryer C. L., Wollaeger R. T., Belczynski K., Even W., Kouveliotou C., 2023, *ApJ*, 956, 71

Kaneko Y., Preece R. D., Briggs M. S., Paciesas W. S., Meegan C. A., Band D. L., 2006, *ApJS*, 166, 298

Kann D. A. et al., 2019, *A&A*, 624, A143

Kara E., Miller J. M., Reynolds C., Dai L., 2016, *Nature*, 535, 388

Kawakubo Y. et al., 2025, GRB Coordinates Network, 40910, 1

Kennea J. A., Siegel M. H., Evans P. A., Page K. L., O'Connor B., Swift Team, 2025, GRB Coordinates Network, 40919, 1

Klebesadel R. W., Laros J. G., Fenimore E. E., 1984, *BAAS*, 16, 1016

Kobayashi S., Piran T., Sari R., 1997, *ApJ*, 490, 92

Kocevski D. et al., 2018, *ApJ*, 862, 152

Krimm H. et al., 2011a, *Astron. Telegram*, 3384, 1

Krimm H. et al., 2011b, *Astron. Telegram*, 3463, 1

Krolík J. H., Piran T., 2011, *ApJ*, 743, 134

Kumar A. et al., 2025, GRB Coordinates Network, 40908, 1

Lawrence D. J. et al., 2025, *Space Sci. Rev.*, 221, 78

Levan A. J. et al., 2011, *Science*, 333, 199

Levan A. J. et al., 2014, *ApJ*, 781, 13

Levan A. J. et al., 2024, *Nature*, 626, 737

Levan A. J. et al., 2025a, *ApJ*, 990, L28

Levan A. J. et al., 2025b, GRB Coordinates Network, 40961, 1

Levan A. J. et al., 2025c, GRB Coordinates Network, 41096, 1

Li D. Y., Yang J., Zhang W. D., the Einstein Probe collaborations, 2025a, preprint (arXiv:2509.25877)

Li X. et al., 2025b, GRB Coordinates Network, 40986, 1

Lin R. P. et al., 1995, *Space Sci. Rev.*, 71, 125

Linden T., Valsecchi F., Kalogera V., 2012, *ApJ*, 748, 114

Lithwick Y., Sari R., 2001, *ApJ*, 555, 540

MacFadyen A. I., Woosley S. E., 1999, *ApJ*, 524, 262

Maeda K., Moriya T. J., 2022, *ApJ*, 927, 25

Martin-Carrillo A. et al., 2025, GRB Coordinates Network, 40924, 1

Masterson M. et al., 2025, *Nature*, 638, 370

Matsuoka M. et al., 2009, *PASJ*, 61, 999

Mazets E. P. et al., 2008, *ApJ*, 680, 545

Meegan C. et al., 2009, *ApJ*, 702, 791

Metzger B. D., 2012, *MNRAS*, 419, 827

Metzger B. D., 2022, *ApJ*, 932, 84

Morales-Rivera G., Gill R., Arthur S. J., Beniamini P., Granot J., 2025, *MNRAS*, preprint (arXiv:2508.03689)

Negro M., Younes G., Wadiasingh Z., Burns E., Trigg A., Baring M., 2024, *Front. Astron. Space Sci.*, 11, 1388953

Neights E., Roberts O. J., Burns E., Veres P., Fermi-GBM Team, 2025a, GRB Coordinates Network, 40891, 1

Neights E., Roberts O. J., Burns E., Veres P., Bissaldi E., Fermi-GBM Team, 2025b, GRB Coordinates Network, 40931, 1

Nishio H. et al., 2025, *Astron. Telegram*, 17260, 1

Norris J. P., Bonnell J. T., 2006, *ApJ*, 643, 266

Norris J. P., Marani G. F., Bonnell J. T., 2000, *ApJ*, 534, 248

O'Connor B. et al., 2023, *Sci. Adv.*, 9, eadi1405

O'Connor B. et al., 2025, *ApJ*, 994, L17

O'Connor B., Pasham D., Andreoni I., Hare J., 2025, GRB Coordinates Network, 41014, 1

Oganesyan G. et al., 2025, *A&A*, 703, L2

Paczynski B., 1986, *ApJ*, 308, L43

Panque D. et al., 2025, GRB Coordinates Network, 41067, 1

Parsotan T., Lazzati D., 2024, *ApJ*, 974, 158

Perets H. B., Li Z., Lombardi J. C. Jr., Milcarek S. R. Jr., 2016, *ApJ*, 823, 113

Pérez-García I. et al., 2025, GRB Coordinates Network, 40929, 1

Perna R., Lazzati D., Cantiello M., 2018, *ApJ*, 859, 48

Piran T., 1999, *Phys. Rep.*, 314, 575

Planck Collaboration VI, 2020, *A&A*, 641, A6

Poolakkil S. et al., 2021, *ApJ*, 913, 60

Rastinejad J. et al., 2021, *ApJ*, 916, 89

Rastinejad J. C. et al., 2022, *Nature*, 612, 223

Rastinejad J. C. et al., 2025, *ApJ*, 988, L13

Ravasio M. E., Oganesyan G., Ghirlanda G., Nava L., Ghisellini G., Pescalli A., Celotti A., 2018, *A&A*, 613, A16

Rees M. J., 1988, *Nature*, 333, 523

Roberts O. J., Burns E., Fermi-GBM Team, 2024, GRB Coordinates Network, 38184, 1

Rosswog S., Ramirez-Ruiz E., Hix W. R., 2009, *ApJ*, 695, 404

Rueda J. A., Ruffini R., Li L., Moradi R., Sahakyan N., Wang Y., 2023, in Ruffino R., Vereshchagin G., eds, The Sixteenth Marcel Grossmann Meeting. On Recent Developments in Theoretical and Experimental General Relativity, Astrophysics, and Relativistic Field Theories. World Scientific, Singapore, p. 217

Sakamoto T. et al., 2011, GRB Coordinates Network, 11842, 1

Schulze S. et al., 2025, *Nature*, 644, 634

Scotton L., Piron F., Omodei N., Di Lalla N., Bissaldi E., 2023, *ApJ*, 956, 101

Sfaradi A. I. et al., 2025, GRB Coordinates Network, 41053, 1

Shakura N. I., Sunyaev R. A., 1973, *A&A*, 24, 337

Siegel M. H., Swift/UVOT Team, 2025, GRB Coordinates Network, 40952, 1

Stratta G. et al., 2013, *ApJ*, 779, 66

SVOM/GRM Team, 2025, GRB Coordinates Network, 40923, 1

Tang Q.-W., Peng F.-K., Wang X.-Y., Tam P.-H. T., 2015, *ApJ*, 806, 194

Thompson C., Duncan R. C., 1995, *MNRAS*, 275, 255

Thöne C. C. et al., 2011, *Nature*, 480, 72

Tikhomirova Y. Y., Stern B. E., 2005, *Astron. Lett.*, 31, 291

Timmer J., König M., 1995, *A&A*, 300, 707

Tohuvavohu A., Kennea J. A., DeLaunay J., Palmer D. M., Cenko S. B., Barthelmy S., 2020, *ApJ*, 900, 35

Tomsick J. et al., 2024, in Saito T., Okumura K., eds, Proc. Sci., 38th International Cosmic Ray Conference, The Compton Spectrometer and Imager. Nagoya, Japan, p. 745

Trigg A. C. et al., 2025, *A&A*, 694, A323

Tsvetkova A. et al., 2017, *ApJ*, 850, 161

Tsvetkova A. et al., 2021, *ApJ*, 908, 83

Ukwatta T. N. et al., 2010, *ApJ*, 711, 1073

Van den Heuvel E., Eggleton P., 1976, in Eggleton P., Mitton S., Whelan J., eds, Proc. IAU Symp. 73, Structure and Evolution of Close Binary Systems. Kluwer, Dordrecht, p. 35

Vaughan S., 2005, *A&A*, 431, 391

Vaughan S., 2010, *MNRAS*, 402, 307

Veres P. et al., 2023, *ApJ*, 954, L5

Vianello G., Gill R., Granot J., Omodei N., Cohen-Tanugi J., Longo F., 2018, *ApJ*, 864, 163

Vreeswijk P., Fynbo J., Melandri A., 2011, GRB Coordinates Network, 12648, 1

Wilkins D. R., 2019, *MNRAS*, 489, 1957

Wu Z.-F., Damoulakis M., Beniamini P., Giannios D., 2025, *ApJ*, 980, L28

Yassine M., Piron F., Mochkovitch R., Daigne F., 2017, *A&A*, 606, A93

Zhang W., Fryer C. L., 2001, *ApJ*, 550, 357

Zhang B., Fan Y. Z., Dyks J., Kobayashi S., Mészáros P., Burrows D. N., Nousek J. A., Gehrels N., 2006, *ApJ*, 642, 354

Zhang J.-P. et al., 2025, preprint (arXiv:2509.26283)

Zou Y.-C., Fan Y.-Z., Piran T., 2011, *ApJ*, 726, L2

APPENDIX A: GRB 250702B LIGHT CURVE AND BACKGROUND AND SOURCE SELECTIONS

Determining the light curve of GRB 250702B requires the development of a self-consistent set of background determinations across instruments as well as intervals of significant emission. We use additional information in order to determine when significant fluctuations are due specifically to GRB 250702B. The evidence in total is summarized in Fig. A1. Subsection A1 details the background fitting, subsection A2 the source selections, and subsection A3 the searches for gamma-ray emission in wider intervals.

A1 Background

Swift-BAT creates sky-images using the balanced mask-weighted technique that automatically subtracts out background. The *Psyche*-GRNS background is an average from the counts between T0-25 000 s to T0+20 000 s and T0+120 000 s to T0 + 165 000 s. The method for determining Konus-Wind and *Fermi*-GBM backgrounds are more complex and detailed below.

A1.1 Konus-Wind

In the waiting mode both Konus-Wind (KW) detectors measure count rates in three energy bands (called G1, G2, and G3), with

the following energy boundaries: 23–96 keV, 96–398 keV, and 398–1628 keV in the S1 detector, and 18–76 keV, 76–316 keV, and 316–1250 keV in the S2 detector. Long-time-scale count rate variations in G1 are mostly related to the galactic X-ray transient activity, while G2 and G3 background variations are typically produced by variations in the solar energetic particle (protons and electrons) flux.

We investigate Konus background behaviour during the interval between T0-172,800 s and T0 + 25,9200 s, with the S2 waiting mode data shown in Fig. A2. The average count rates are \sim 1018 counts/s (G1), \sim 340 counts/s (G2), \sim 107 counts/s (G3). Typical long-term variations in background rate are \sim 10 counts/s (G1), \sim 5 counts/s (G2), and \sim 2 counts/s (G3). In the G2 and G3 bands there is a step-like feature with an amplitude of \sim 2 and \sim 4 counts/s, respectively, around T0 + 55,020 s, which is related to a drop in proton and electron flux seen in 3DP-Wind (R. P. Lin et al. 1995).

To estimate background rates for GRB 250702B, we limit our analysis to the interval between T0+39 518 s (end of the data gap after the GRB 250702A readout) and T0 + 75 847 s (just before GRB 250702F). We select the background interval using Bayesian block decomposition of the light curves in each energy band and fit the background using three models: a constant count rate (a) in G1, a linear model ($a + bt$) in G2, and a logistic function ($a + b/(1 + e^{c(t-t_0)})$) in G3. The model parameters are given in Table A1.

A1.2 *Fermi*-GBM

Typically, the time-variable background of a GRB detected by *Fermi*-GBM is estimated by fitting a polynomial to the count rate during time intervals before and after the burst (e.g. S. Poolakkil et al. 2021). This method does not work well for very long-duration events, such as GRB 250702B, because the background may fluctuate more than can be modelled with a simple polynomial, and faint source emission may contaminate the time intervals selected as background.

An alternative background estimation method is to use background rates from orbits preceding and/or following that of the long-duration burst observation (G. Fitzpatrick et al. 2011), and we adopt both this approach and the traditional polynomial method. Charged particles are a significant source of background for *Fermi*-GBM, meaning that the rate and spectrum of the background vary with the geographic position. Further, the directional-dependent response means background also depends on the orientation of the satellite. The background at a given time t_0 can be estimated using observations when the spacecraft returns to the same position and orientation as at t_0 .

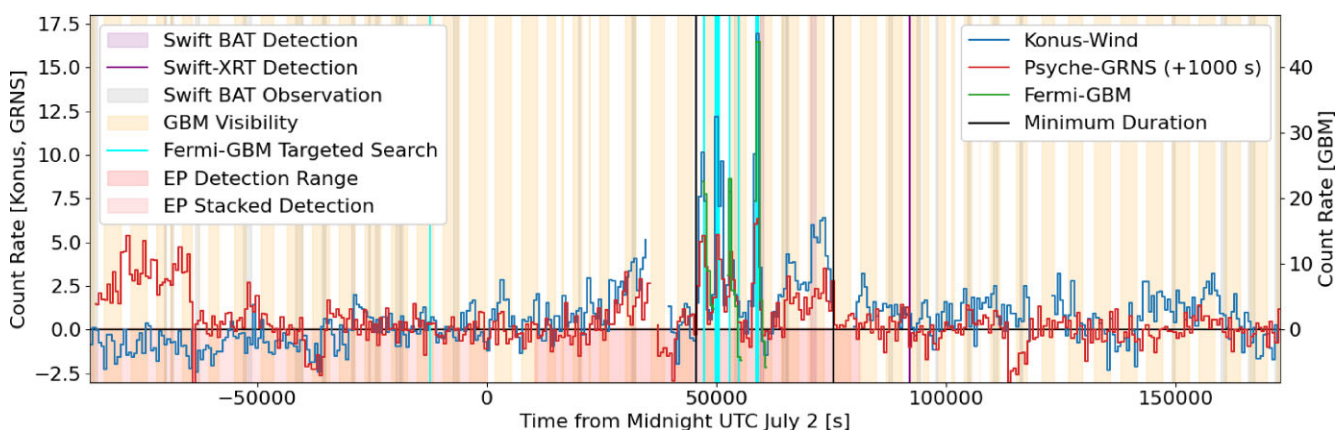


Figure A1. The combined light curves and additional detection information utilized to determine the prompt gamma-ray emission times.

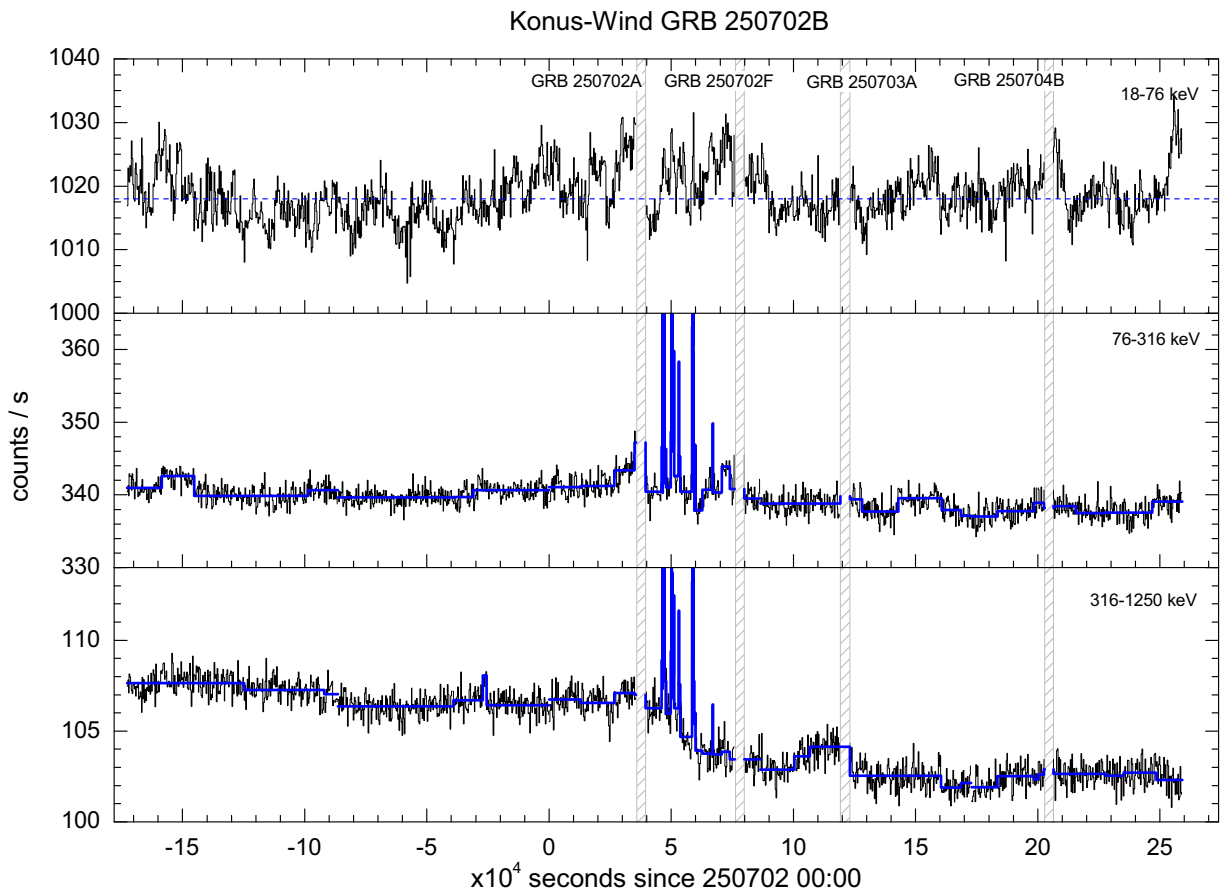


Figure A2. The Konus-Wind S2 waiting mode data between $T_0 - 172,800$ s and $T_0 + 259,200$ s. The blue solid lines in the G2 and G3 panels indicate Bayesian block binning, the blue dashed line in the G1 panel is the mean count rate, and the grey hatched intervals are data readout intervals for triggered GRBs, during which Konus did not collect data.

The *Fermi* spacecraft returns to the same geographic position every 15 orbits. Because the satellite alternates its pointing every two orbits, this gives two options to estimate the background: 1) using the observations at $t_0 \pm 30$ orbits, which is at approximately $t_0 \pm 48$ h, or 2) averaging the observations at $t_0 \pm 14$ and $t_0 \pm 16$ orbits, when the detector orientation is correct, but the geographic positions are slightly offset from that at $t_0 \pm 15$ orbits.

We estimate the background for the duration of interest from $T_0 + 45,600$ s to $T_0 + 61,800$ s. The orientation of *Fermi* was modified due to a Target of Opportunity observation leading up to GRB 250702B. Therefore, it is infeasible to use observations until *Fermi* resumed its nominal observation mode at around $T_0 + 27,900$ s to estimate the background. Thus, we estimate the background using the observation at $T_0 + 30$ orbits, between $T_0 + 215,685$ s and $T_0 + 231,885$ s. We do not expect any unrelated transients to interfere with the background estimation at energies $\gtrsim 100$ keV, since *Fermi*-GBM did not trigger on any astrophysical transients during this time.

The background light curve evolution extracted from $T_0 + 30$ orbits overall matches that of the GRB 250702B interval, although there are offsets in normalization, as seen in Fig. A3. To resolve this, we select normalization time intervals during which GRB 250702B is occulted by the Earth or Konus detects < 10 counts/bin in the G1 detector and < 5 counts/bin in G2 outside of the GBM analysis intervals, in order to minimize source contamination. We add an additional interval between Interval 4 and the SAA passage of *Fermi*

because the light curve profile differs significantly between the source and orbital background intervals leading up to the SAA. However, there is likely emission (especially soft) from GRB 250702B at this time, which may impact the background estimation and spectral analysis results for Interval 4. The normalization intervals are broken up into time periods of < 200 s. A normalization factor is calculated for each detector, energy channel, and normalization interval by dividing the source and background counts. Using linear interpolation, normalization factors throughout the GRB 250702B interval at 1 s resolution are computed. Fig. A3 shows a much improved estimate of the overall background rate using this additional scaling step. The background-subtracted light curve matches that of Konus-Wind and *Psyche*-GRNS, as shown in Fig. 1, validating the background estimation. To estimate the background for spectral analysis, we fit and normalize a polynomial to the orbital background during and around each GBM analysis interval, with the time intervals listed in Table A2.

As a cross-check, we additionally estimate the background via the usual polynomial fitting method. Using the *Fermi* Gamma-ray Data Tools (GDT-Fermi; A. Goldstein, W. H. Cleveland & D. Kocevski 2023), we fit polynomials to the 5 s binned light curve for each detector and energy channel in intervals before and after each analysis interval described in Appendix A2.2 and summarized in Table A7. The background is fit with an order 1 polynomial for all intervals except for GBM Interval 5, where an order 2 polynomial is used. The

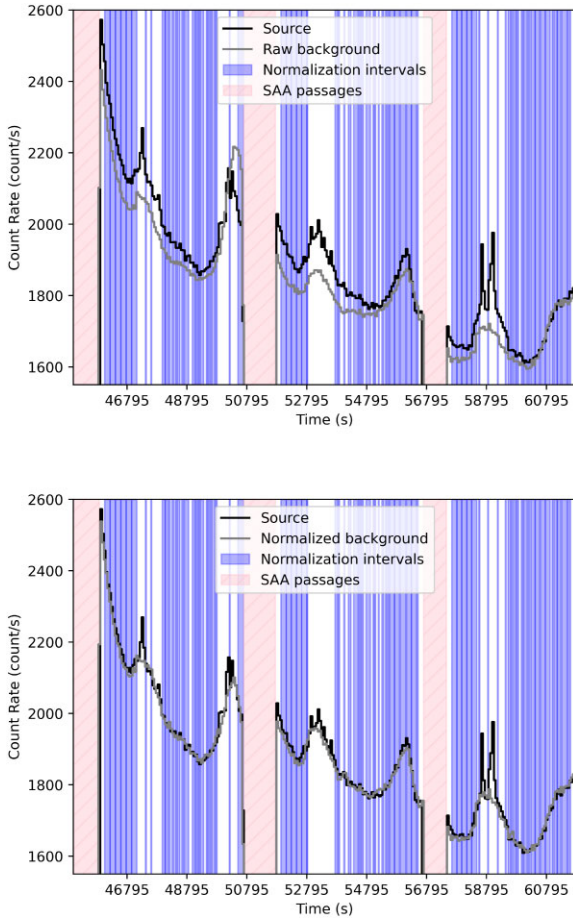


Figure A3. The normalization of *Fermi*-GBM orbital background. *Top*: The raw orbital background overlaid on the source interval light curve. The normalization intervals in blue are used to compute normalization factors. *Bottom*: The normalized orbital background overlaid on the source interval light curve.

polynomial fits for the spectral lag measurements are summarized in Table A3. For spectral analysis, we more carefully choose intervals for polynomial fitting to avoid times when there may be dim GRB 250702B emission which may impact the spectral results, through manual inspection of the GBM and Konus source interval and GBM orbital background light curves. These are displayed in Table A4.

A2 Source selections

The *Psyche*-GRNS data is predominantly used to confirm the signal variability seen in Konus-*Wind*, allowing for the total duration measurement. Konus-*Wind* analysis intervals are selected using Bayesian block decomposition of the G2 light curve. The other instruments have additional source selections, detailed here.

A2.1 Swift-BAT

Swift-BAT is a coded mask imager, capable of creating images of the 14–195 keV sky. On July 2, GRB 250702B was within the coded field-of-view of *Swift*-BAT seven times, with five of those occurring after the initial *Fermi*-GBM trigger. None of these observations overlap with the bright intervals listed in Table A7. There are two

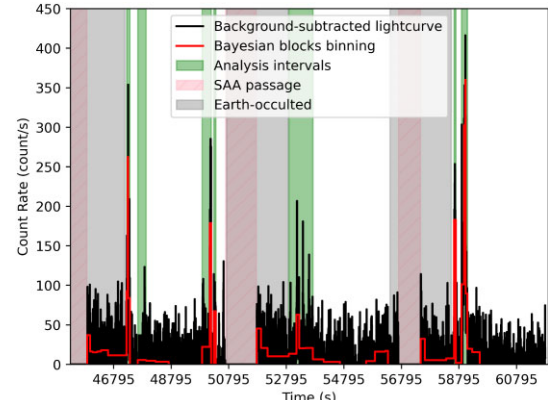


Figure A4. The background-subtracted *Fermi*-GBM light curve binned using Bayesian blocks. The analysis intervals which include bins with $\text{SNR} > 10$ are overlaid.

detections and two non-detections in the main emission, shown in Fig. 1. One detection confirms the later emission seen in Konus and GRNS as arising from this burst, significantly extending the gamma-ray duration.

A2.2 *Fermi*-GBM

Fermi-GBM triggered during the emission from GRB 250702B. All four times contained emission from this event, though one trigger was due to an unrelated short GRB as explained in Section A4. The *Fermi*-GBM onboard triggers associated with GRB 250702B and the relevant detectors are shown in Table A5.

The brightest gamma-ray emission occurs between $\sim T_0 + 46\,074$ s and $\sim T_0 + 61\,800$ s. We bin the *Fermi*-GBM light curve for detectors n7, n8, n9, nb, and b1 in this interval using Bayesian blocks, in the 50–500 keV energy range for the NaI detectors and 400–1000 keV for the BGO detectors. The time periods composed of bins with $\text{SNR} > 10$ are summarized in Table A6. We measure the MVT and spectral lag in each of these intervals as well as perform spectral analysis, finding the peak energy to vary with brightness as is typical for GRBs. In order to constrain spectral curvature in every interval, we merge adjacent bins into a single interval, as displayed in Table A7. The light curve binned using Bayesian blocks is shown in Fig. A4.

There are two additional intervals in which the $\text{SNR} > 10$: $T_0 + 51,765$ – $51,915$ s, and $T_0 + 57,465$ – $57,610$ s. These are believed to be due to poor background estimation at times near the SAA passages of *Fermi*, as described in Section A1.2, and are therefore not included in analysis. The time window containing GRB 250702C, an unrelated short GRB which occurred between $T_0 + 53\,371.46$ s and $T_0 + 53\,371.97$ s, is excised from Interval 5 for analyses.

A3 Extended searches for gamma-ray emission

In order to determine the length of the prompt gamma-ray duration, we perform dedicated searches in *Swift*-BAT, MAXI, and *Fermi*-GBM for emission outside of the main $\sim 25\,000$ s gamma-ray emission interval. As detailed below, in no instrument do we find significant evidence for gamma-ray emission outside of our 25 000 s interval.

Table A1. Konus-Wind background fit results, showing the intervals over which the fit is measured and the model parameters used to estimate the background.

Energy band	Intervals - T0 (s)	Model	Model parameters
G1	59 929–62 690	Constant	$a = 1018.3 \pm 1.6$ (counts/s)
G2	39 518–46 074	Linear	$a = 339.0 \pm 0.4$ (counts/s)
	59 929–62 690		$b = (-1.2 \pm 0.3) \times 10^{-4}$ (counts/s ²)
G3	39 518–46 074	Logistic	$a = 106.36 \pm 0.16$ (counts/s)
	47 958–49 842		$b = -2.58 \pm 0.20$ (counts/s)
	54 297–57 594		$c = (-7 \pm 5) \times 10^{-4}$ (1/s)
	59 929–74 004		$t_0 = (54.4 \pm 1.1) \times 10^3$ (s)

Table A2. Time intervals to which polynomials are fit to *Fermi*-GBM orbital background data for spectral analysis of each interval in Table A7. All polynomials are order 1 except for Interval 5 which is order 3.

GBM interval	Background interval - T0 (s)
1	47 145–47 455
2	47 530–48 020
3	49 765–50 275
4	50 185–50 445
5	52 780–53 815
6	58 525–58 785
7	58 780–59 185

Table A3. Time intervals to which polynomials are fit to *Fermi*-GBM data for spectral lag measurements of the corresponding intervals in Table A6. All polynomials are order 1 except for Interval 5 which is order 2.

GBM Interval	Background Interval Before - T0 (s)	Background Interval After - T0 (s)
1	47 045–47 195	47 405–47 545
2	47 430–47 580	47 970–48 105
3	49 935–50 085	50 210–50 275
4	50 185–50 250	50 370–50 525
5	52 379–52 855	53 765–54 180
6	58 225–58 575	58 735–58 875
7	58 690–58 855	59 134–59 379

Table A4. Time intervals to which polynomials are fit to *Fermi*-GBM data for spectral analysis of the intervals in Table A7. The same ranges are used to fit the background for the corresponding intervals in Table A6. All polynomials are order 1 except for Interval 5, which is order 2.

GBM Interval	Background interval Before - T0 (s)	Background interval After - T0 (s)
1	46 991–47 120	47 408–47 538
2	47 535–47 614	47 968–48 071
3	49 713–49 793	50 205–50 259
4	50 205–50 259	50 475–50 686
5	52 671–52 825	53 738–53 926
6	58 537–58 566	58 831–58 860
7	58 830–58 860	59 155–59 184

Table A5. *Fermi*-GBM triggers comprising GRB 250702B. The positions are calculated from the *Fermi*-GBM trigger data. The good detectors are those with a viewing angle within 60° of the source, which are used in analysis.

Name	Trigger time - T0 (s)	Position (RA, Dec; °)	Good Detectors
250702548	47 342.03	(290, 0) ± 10	n8, nb, b1
250702581	50 165.77	(286, -9) ± 8	n9, na, nb, b1
250702682	58 893.07	(290, -20) ± 10	n8, nb, b1

Table A6. Intervals with SNR > 10 in the Bayesian blocks binned light curve.

GBM interval Name	Time interval - T0 (s)	Good Detectors
1a	47 245–47 285	n8, nb, b1
1b	47 285–47 300	n8, nb, b1
1c	47 300–47 355	n8, nb, b1
2	47 630–47 920	n8, nb, b1
3a	49 865–50 135	n9, na, nb, b1
3b	50 135–50 185	n9, na, nb, b1
4	50 275–50 345	n9, na, nb, b1
5a	52 880–53 150	n7, n8, nb, b1
5b	53 150–53 245	n7, n8, nb, b1
5c	53 245–53 715	n7, n8, nb, b1
5d	53 445–53 715	n7, n8, nb, b1
6	58 625–58 685	n8, nb, b1
7a	58 880–58 975	n8, nb, b1
7b	58 975–58 990	n8, nb, b1
7c	58 990–59 015	n8, nb, b1
7d	59 015–59 030	n8, nb, b1
7e	59 030–59 085	n8, nb, b1

Table A7. Intervals determined using the Bayesian blocks binned light curve in which we perform detailed *Fermi*-GBM analysis. The good detectors are those with a viewing angle within 60° of the source, which are used in analysis. These intervals are shaded on the light curve in Fig. 1.

GBM Interval Name	Time interval - T0 (s)	Good detectors
1	47 245–47 355	n8, nb, b1
2	47 630–47 920	n8, nb, b1
3	49 865–50 185	n9, na, nb, b1
4	50 275–50 345	n9, na, nb, b1
5	52 880–53 715	n7, n8, nb, b1
6	58 625–58 685	n8, nb, b1
7	58 880–59 085	n8, nb, b1

A3.1 Swift-BAT analysis

To search for extended hard X-ray to gamma-ray emission, B. O'Connor et al. (2025) analysed the *Swift*-BAT survey data products from the observations with GRB 250702B in the coded field-of-view. Two significant detections of GRB 250702B were made over observations from T0+59 411 s to T0+60 267 s and from T0+70 549 s to T0 + 71 607 s, as illustrated in Fig. 1. No other significant emission was found in *Swift*-BAT survey data at the position of GRB 250702B from ∼1 month prior to July 2 to ∼4 d after July 2.

Table A8. Detections and non-detections around the time of GRB 250702B by MAXI in the 2–20 keV energy range.

Start time - T0 (s)	Stop time - T0 (s)	Detection
2451	2519	No
8026	8095	No
13 590	13665	No
19 174	19 243	No
24 744	24 816	No
30 319	30 390	No
35 886	35 959	No
41 461	41 534	No
47 035	47 107	Yes
52 614	52 688	Yes
58 181	58 254	Yes
63 762	63 835	No
69 335	69 408	No
74 909	74 983	No
80 481	80 555	No
86 055	86 131	No

A3.2 MAXI analysis

We searched for significant emission in the 2–20 keV energy range in MAXI on 2025 July 2. We find only three intervals with signals over 2σ , consistent with initial reporting (Y. Kawakubo et al. 2025). Detections and non-detections are summarized in Table A8.

A3.3 *Fermi*-GBM targeted search results

GBM has developed increased sensitivity to transient signals lying below the onboard triggering algorithms by means of subthreshold searches. The Targeted Search was developed for multimessenger follow-up (L. Blackburn et al. 2015), and is currently used to identify subthreshold GRB emission triggered by other instruments, such as *Swift*-BAT (D. Kocevski et al. 2018) and the ECLAIRS telescope onboard the *Space-based multiband astronomical Variable Objects Monitor* (e.g. E. Burns et al. 2024, O. J. Roberts, E. Burns & Fermi-GBM Team 2024). The Targeted Search processes continuous time-tagged event data from all 14 detectors coherently around an input time. Three model spectra (A. Goldstein et al. 2016) are folded through the detector responses to produce templates of expected counts, which are then compared to the observed distribution of counts in each energy channel of each detector. The comparison is performed via a log-likelihood ratio (LLR), testing the alternative hypothesis of the presence of a signal with a similar spectrum versus the null hypothesis of only background noise. Treating the LLR as our detection statistic, the model spectrum resulting in the highest LLR is selected as the preferred spectrum, and this procedure is repeated for each bin of data in the search. For more details on the Targeted Search method, see L. Blackburn et al. (2015), A. Goldstein et al. (2016), A. Goldstein et al. (2019).

To search for gamma-ray emission from GRB 250702B, we run the Targeted Search from T0-86,460 s to T0 + 345,659 s over periods of time when the source is visible to *Fermi*-GBM, i.e. not in the South Atlantic Anomaly (SAA) and not Earth-occulted. The search is run using overlapping segments of 300 s and processing time-scales from 64 ms to 32.768 s increasing by factors of 2. As performed in standard GBM follow-up, significant events found with the soft spectral template on the 8 s time-scale are removed to limit contamination from non-GRB sources (A. Goldstein et al. 2019).

We find a total of 93 significant candidates, but using a cut on the spatial association probability of ≥ 85 per cent, we reduce the

Table A9. Candidate subthreshold detections of GRB 250702B by the GBM Targeted Search, where the start times are relative to midnight July 2. LLR is the log-likelihood ratio and p_{spatial} is the spatial p -value.

Start time - T0 (s)	Time-scale	Spectrum	LLR	p_{spatial}
-12 294.428	32.768	Soft	14.78	97.8
47 285.332	16.384	Hard	113.50	98.3
50 182.596	4.096	Normal	32.21	94.0
50 168.452	0.128	Soft	14.69	88.9
52 916.956	32.768	Hard	20.38	93.8
54 900.036	32.768	Soft	25.07	98.3
58 636.644	32.768	Hard	98.69	99.3
58 665.316	16.384	Normal	47.68	98.3
271 823.34	32.768	Soft	59.88	99.2

sample to 38 candidates. We then perform a manual inspection of the light curves, localization maps, and spacecraft orbital locations to determine the nature of the candidate. Excluding known GBM triggers, we find nine candidates consistent with the location and spectral nature of GRB 250702B, detailed in Table A9.

There is a possible signal associated with GRB 250702B found on July 1, and another on July 5. In order to estimate the significance of these candidates, we run the identical search settings over ~ 5 Ms of randomly sampled livetime to generate a background distribution. For every candidate event found with the Targeted Search, a skymap is generated, which includes a systematic localization error. Using these skymaps, we calculate a spatial p -value utilizing GDT-Fermi. This spatial check is important because the source position is near the Galactic centre, where we expect an excess of soft and long signals from unrelated sources. We assign a ranking statistic for each candidate as the log-likelihood ratio times the spatial p -value. The more significant of the two is the event on July 5. We find a false alarm rate of 4.5×10^{-5} Hz. However, over a multiday time range, this event is not significant. Given the lack of signal in BAT, we find no convincing evidence for gamma-ray duration beyond the 25 000 s bright interval on July 2nd. J.-P. Zhang et al. (2025) and D. Y. Li et al. (2025a) report a *Fermi*-GBM signal associated with GRB 250702B at 11:55 UTC on July 1. While a candidate detection was found by Targeted Search at this time, it cannot be unambiguously associated with the GRB due to an active X-ray binary, XTE J1858 + 034 (H. Nishio et al. 2025), also appearing within the localization region of the signal.

A4 GRB 250702C dissociation

During the initial reporting of GRB 250702B there were four separate *Fermi*-GBM triggers whose real-time localizations suggested a common origin (E. Neights et al. 2025a). Follow-up analysis dissociated one trigger, assigning it to a separate burst, GRB 250702C (E. Neights et al. 2025b). The confusion arises because GRB 250702C, a short GRB, lies on top of a long interval of emission from GRB 250702B, corresponding to our GBM Interval 5. By convention, GBM onboard triggers are catalogued according to the specific emission responsible for the trigger, even if there is contemporaneous emission from another source at this time and thus this trigger is GRB 250702C.

The confusion arose because the automated *Fermi*-GBM localization software (A. Goldstein et al. 2020) selects the dominant emission around the trigger time, which in this case was actually due to GRB 250702B. Manual analysis at fine time resolution around the specific trigger time identified a very short and significant pulse right at trigger time, as displayed in Fig. A5. Localization shows it originated from a different position on the sky. Thus, it is a separate burst that happened to occur on top of emission from GRB 250702B.

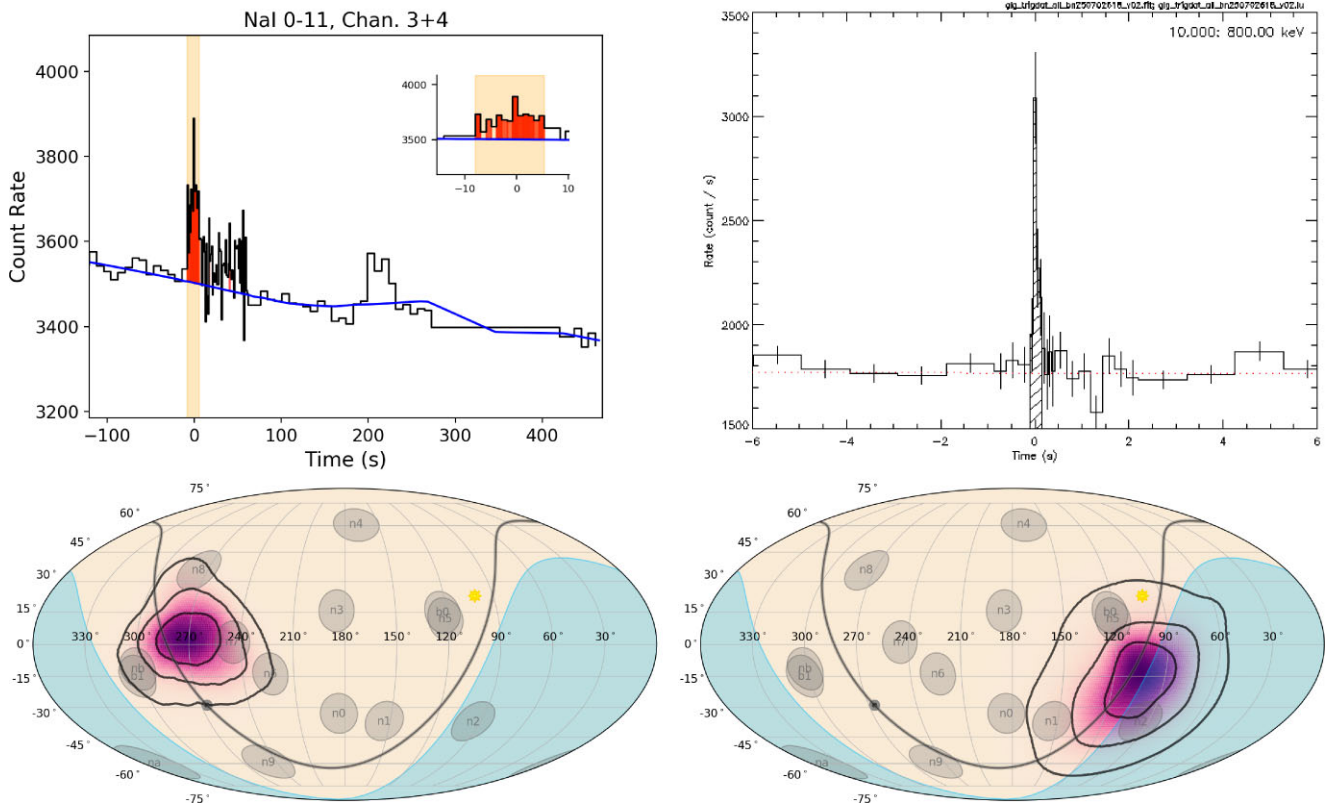


Figure A5. *Left:* the automated *Fermi*-GBM light curve selection and localization of the trigger now assigned to GRB 250702C. *Right:* the manual light curve selection on the short burst GRB 250702C. The longer emission from GRB 250702B dominated the photon counts and pulled the localization to this source, despite the trigger burst originating from a different localization.

APPENDIX B: ADDITIONAL ANALYSIS AND INFERENCE DETAILS

Section 2 contains the key results from the gamma-ray analysis. However, the details of these analyses are sometimes contained here.

B1 Minimum variability time-scale

Here, we display plots showing the measurement of key MVT values. The lowest MVT measured for GRB 250702B and the MVT measurement of *Swift* J1644+57 are shown in Fig. B1. We show the measured MVT from the *Swift*-BAT GUANO intervals of GRB 250702B in Table B1.

B2 Spectral analysis

We here detail the spectral analysis of GRB 250702B in *Fermi*-GBM and Konus-Wind. For comparison, the Konus intervals map on to the GBM intervals in the following way: Konus 1 → GBM 1 and 2, Konus 2 → GBM 3 and 4, Konus 3 → GBM 5, and Konus 4 → GBM 6 and 7, as visualized in Fig. 1.

B2.1 *Fermi*-GBM

We perform time-integrated spectral analysis for each interval in Table A7, using the detectors with observing angles within 60° of the GRB 250702B position and data binned at 5 s resolution. Both the orbital background method and polynomial fitting are used to estimate the background, and we compare the results from these two

methods. Most spectral fits with the polynomial background use the standard energy selection of 8–900 keV for the NaI detectors and 280 keV–40 MeV for the BGO detectors. However, the polynomial background estimation in Interval 3 is problematic $\lesssim 75$ keV, and we therefore perform spectral analysis using 75–900 keV for the NaI detectors. The orbital background is not reliable at low energies, which may be due to interfering point sources and/or weak soft emission from GRB 250702B outside of the known intervals. We thus use energy ranges of 75–900 keV in Intervals 2 and 3, 100–900 keV in Interval 4, and 50–900 keV in the other intervals for the NaI detectors, and 280 keV–40 MeV for the BGO detectors.

A forward-folding analysis is performed using GDT-Fermi, in which a spectral model is convolved with the detector response matrix. The detector response represents the relationship between the incident energies of photons and observed counts in the detector energy channels of *Fermi*-GBM for a particular observation. The GRB 250702B position determined by *Swift*-XRT (J. A. Kennea et al. 2025) is used when computing the detector response matrices. The result of the convolution, which is the expected energy distribution of source counts based on the model, is combined with the background estimate. This is compared with the measured data using the PG statistic (pgstat; K. Arnaud, B. Dorman & C. Gordon 1999), which assumes a Poisson signal and Gaussian background.

The following spectral models are fit where $N(E)$ is the photon spectrum and E is the photon energy:

(i) power law (PL):

$$N(E) = A \left(\frac{E}{E_{\text{piv}}} \right)^\alpha \quad (\text{B1})$$

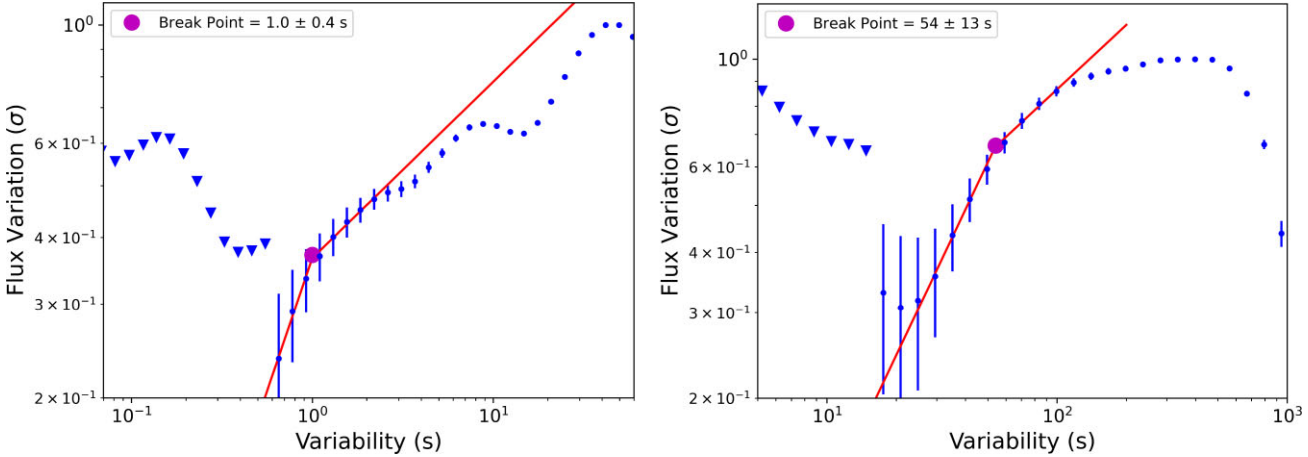


Figure B1. The flux variation as a function of variability time-scale for T0+50 068-50 359 s (left), the time interval that yields the smallest MVT of GRB 250702B, and *Swift* J1644 + 57 (right). A broken power law is fit to these data, with the break point corresponding to the MVT.

where the free parameters are amplitude A and photon index α . The pivot energy E_{piv} is fixed to 100 keV, following S. Poolakkil et al. (2021).

(ii) blackbody (BB):

$$N(E) = A \frac{E^2}{e^{\frac{E}{kT}} - 1} \quad (\text{B2})$$

where the free parameters are amplitude A and blackbody temperature kT .

(iii) cut-off power law (CPL), also known as Comptonized:

$$N(E) = A \left(\frac{E}{E_{\text{piv}}} \right)^\alpha e^{(2+\alpha) \frac{E}{E_p}} \quad (\text{B3})$$

where the free parameters are amplitude A , photon index α , peak energy of the νF_ν spectrum E_p . The pivot energy E_{piv} is fixed to 100 keV.

(iv) Band function (D. Band et al. 1993):

$$N(E) = A \begin{cases} \left(\frac{E}{E_{\text{piv}}} \right)^\alpha e^{-(2+\alpha) \frac{E}{E_p}} & \text{if } E \leq \xi E_p \\ \left(\frac{E}{E_{\text{piv}}} \right)^\beta \left(\xi \frac{E_p}{E_{\text{piv}}} \right)^{\alpha-\beta} e^{\beta-\alpha} & \text{if } E > \xi E_p \end{cases} \quad (\text{B4})$$

where $\xi = \frac{\alpha-\beta}{2+\alpha}$. The free parameters are amplitude A , low-energy photon index α , high-energy photon index β , and peak energy of the νF_ν spectrum E_p . The pivot energy E_{piv} is fixed to 100 keV.

(v) smoothly broken power law (SBPL; Y. Kaneko et al. 2006):

$$N(E) = A \left(\frac{E}{E_{\text{piv}}} \right)^b 10^{a-a_{\text{piv}}} \quad (\text{B5})$$

where $a = mn \ln \left(\frac{e^q + e^{-q}}{2} \right)$, $a_{\text{piv}} = mn \ln \left(\frac{e^{q_{\text{piv}}} + e^{-q_{\text{piv}}}}{2} \right)$, $q = \log(\frac{E}{E_b})/n$, $q_{\text{piv}} = \log(\frac{E_{\text{piv}}}{E_b})/n$, $m = (\beta - \alpha)/2$, and $b = (\alpha + \beta)/2$. The free parameters are amplitude A , low-energy photon index α , high-energy photon index β , and break energy E_b . The smoothness parameter n is fixed to 0.3, following S. Poolakkil et al. (2021).

Table B1. *Swift*-BAT MVT results for GRB 250702B.

Interval - T0 (s)	MVT (s)
47 323–47 355	< 5.48
53 355–53 555	< 40.27
58 880–59 075	6.8 ± 0.9

(vi) double smoothly broken power law (2SBPL; M. E. Ravasio et al. (2018)):

$$N(E) = A E_b^{\alpha_1} \left(\left(\frac{E}{E_b} \right)^{-\alpha_1 n_1} + \left(\frac{E}{E_b} \right)^{-\alpha_2 n_1} \right)^{\frac{n_2}{n_1}} + \left(\frac{E}{E_j} \right)^{-\beta n_2} \left(\left(\frac{E_j}{E_b} \right)^{-\alpha_1 n_1} + \left(\frac{E_j}{E_b} \right)^{-\alpha_2 n_1} \right)^{\frac{n_2}{n_1}} \quad (\text{B6})$$

where $E_j = (- (2 + \alpha_2)/(2 + \beta))^{1/n_2(\beta - \alpha_2)} E_p$. The free parameters are amplitude A , low-energy photon index α_1 , photon index between the break and peak energies α_2 , high-energy photon index β , peak energy E_p , and break energy E_b . The break energy smoothness parameter n_1 is fixed to 5.38, and the peak energy smoothness parameter n_2 is fixed to 2.69, following M. E. Ravasio et al. (2018).

We also test the following models: Band function with an exponential cut-off (G. Vianello et al. 2018), Band function with a SBPL (G. Vianello et al. 2018), PL+BB, CPL+BB, Band + BB (S. Guiriec et al. 2011), and SBPL + BB. These do not yield solid constraints and are never statistically preferred, so they are excluded from the results.

The results for all successful time-integrated fits of each analysis interval are in Tables B2, B3, B4, B5, B6, B7, and B8, with the best fit models summarized in Table 3. We also perform spectral analysis for two peak flux intervals: T0+59,024.082–59,025.106 s and T0 + 50,163.206–50,164.230 s using the Interval 3 and 7 backgrounds, respectively. The results are summarized in Table B9 and Table B10. The T0 + 50,163.206–50,164.230 s peak flux spectral results are plotted in Figs B2 and B3. Contrary to the usual GBM standard, we report fluences and fluxes in the 1–10 000 keV bolometric range, which cannot be directly compared with the values in the GBM catalogue. Due to difficulties estimating the background in Intervals 3 and 4, we caution against drawing strong inferences from those measurements, including the Interval 3 peak flux results. The Interval 2 and 5 spectra are also unreliable because they consist of dim emission over a long time period.

G. Oganesyan et al. (2025) analyse *Fermi*-GBM data to study GRB 250702B. Their spectral analysis also contains both orbital background and polynomial background approaches. They probe the three brightest intervals in GBM corresponding to the triggers and report a best-fitting spectrum of a power-law in all cases. The orbital background utilized for their third fit interval uses background

Table B2. Spectral analysis results for Interval 1 using *Fermi*-GBM detectors n8, nb, and b1. The fluence is given in the 1–10 000 keV range. Uncertainties are given at the 90 per cent confidence level. For the NaI detectors, we use an energy range of 50–900 keV with the orbital background and 8–900 keV with the polynomial background. CPL is the preferred model with both the orbital and polynomial background.

Background	Model	α	β	E_p (keV)	E_b/kT (keV)	Stat/ DOF	Fluence (erg cm $^{-2}$)
Orbital	PL	$-1.40^{+0.03}_{-0.03}$				451/303	$1.06^{+0.07}_{-0.06} \times 10^{-4}$
	BB				582^{+11}_{-12}	521/303	$2.144^{+0.07}_{-0.08} \times 10^{-4}$
	CPL	$-0.71^{+0.04}_{-0.05}$		3400^{+400}_{-300}		327/302	$1.69^{+0.05}_{-0.06} \times 10^{-4}$
Polynomial	PL	$-1.40^{+0.04}_{-0.04}$				301/361	$6.6^{+0.5}_{-0.4} \times 10^{-5}$
	CPL	$-1.22^{+0.08}_{-0.08}$		3500^{+200}_{-2000}		286/360	$6.1^{+0.6}_{-0.5} \times 10^{-5}$
	SBPL	$-1.24^{+0.08}_{-0.08}$	$-1.9^{+0.2}_{-0.6}$		900^{+1000}_{-500}	283/359	$5.9^{+0.5}_{-0.4} \times 10^{-5}$

Table B3. Spectral analysis results for Interval 2 using *Fermi*-GBM detectors n8, nb, and b1. The fluence is given in the 1–10 000 keV range. Uncertainties are given at the 90 per cent confidence level. For the NaI detectors, we use an energy range of 75–900 keV with the orbital background and 8–900 keV with the polynomial background. BB is the preferred model with the orbital background and CPL is the preferred model with the polynomial background.

Background	Model	α	β	E_p (keV)	E_b/kT (keV)	Stat/ DOF	Fluence (erg cm $^{-2}$)
Orbital	PL	$-1.35^{+0.03}_{-0.03}$				836/284	$1.25^{+0.08}_{-0.09} \times 10^{-4}$
	BB				694^{+12}_{-13}	442/284	$3.89^{+0.14}_{-0.13} \times 10^{-4}$
	CPL	$1.44^{+0.03}_{-0.03}$		2670^{+60}_{-70}		445/283	$3.90^{+0.13}_{-0.14} \times 10^{-4}$
Polynomial	PL	$-1.22^{+0.11}_{-0.2}$				435/361	$2.3^{+0.6}_{-0.9} \times 10^{-5}$
	CPL	$2.7^{+0.2}_{-0.3}$		2200^{+200}_{-300}		425/360	$5.9^{+0.7}_{-4} \times 10^{-5}$

Table B4. Spectral analysis results for Interval 3 using *Fermi*-GBM detectors n9, na, nb, and b1. The fluence is given in the 1–10 000 keV range. Uncertainties are given at the 90 per cent confidence level. For the NaI detectors, we use an energy range of 75–900 keV with the orbital background and 75–900 keV with the polynomial background. CPL is the preferred model with the orbital background and PL is the preferred model with the polynomial background.

Background	Model	$\alpha/$ $\alpha_1; \alpha_2$	β	E_p (keV)	E_b/kT (keV)	Stat/ DOF	Fluence (erg cm $^{-2}$)
Orbital	PL	$-1.37^{+0.03}_{-0.03}$				698/366	$1.42^{+0.08}_{-0.08} \times 10^{-4}$
	CPL	$-0.10^{+0.04}_{-0.04}$		2700^{+800}_{-800}		449/365	$2.62^{+0.12}_{-0.12} \times 10^{-4}$
	Band	$-0.10^{+0.04}_{-0.05}$	-5^{+2}_{-5}	2700^{+200}_{-200}		449/364	$2.63^{+0.12}_{-0.13} \times 10^{-5}$
	2SBPL	$-0.453^{+0.013}_{-0.014}; -0.68^{+0.11}_{-0.12}$	-6^{+2}_{-3}	3000^{+300}_{-300}	400^{+300}_{-200}	430/362	$2.8^{+0.2}_{-0.2} \times 10^{-4}$
Polynomial	PL	$-1.50^{+0.05}_{-0.06}$				585/366	$9.8^{+0.9}_{-0.7} \times 10^{-5}$
	BB				79^{+2}_{-2}	630/366	$1.99^{+0.09}_{-0.10} \times 10^{-5}$
	SBPL	$-1.34^{+0.12}_{-0.14}$	$-1.60^{+0.12}_{-0.2}$		400^{+1000}_{-300}	583/364	$9.4^{+1.1}_{-0.9} \times 10^{-5}$

Table B5. Spectral analysis results for Interval 4 using *Fermi*-GBM detectors n9, na, nb, and b1. The fluence is given in the 1–10 000 keV range. Uncertainties are given at the 90 per cent confidence level. For the NaI detectors, we use an energy range of 100–900 keV with the orbital background and 8–900 keV with the polynomial background. CPL is the preferred model with both the orbital and polynomial background.

Background	Model	α	β	E_p (keV)	E_b/kT (keV)	Stat/ DOF	Fluence (erg cm $^{-2}$)
Orbital	PL	$-1.41^{+0.04}_{-0.05}$				305/343	$4.47^{+0.03}_{-0.03} \times 10^{-5}$
	BB				610^{+20}_{-20}	299/343	$8.2^{+0.4}_{-0.5} \times 10^{-5}$
	CPL	$-0.48^{+0.06}_{-0.07}$		3500^{+500}_{-500}		265/342	$7.2^{+0.5}_{-0.5} \times 10^{-5}$
	Band	$-0.47^{+0.07}_{-0.08}$	$-3.6^{+1.3}_{-6}$	3400^{+500}_{-500}		264/341	$7.2^{+0.6}_{-0.6} \times 10^{-5}$
	SBPL	$-0.72^{+0.05}_{-0.06}$	$-9.8^{+3}_{-0.2}$		6300^{+1000}_{-1100}	261/341	$7.4^{+0.5}_{-0.6} \times 10^{-5}$
Polynomial	PL	$-1.42^{+0.05}_{-0.06}$				398/481	$3.0^{+0.3}_{-0.3} \times 10^{-5}$
	CPL	$-1.0^{+0.2}_{-0.2}$		530^{+200}_{-120}		386/480	$9.7^{+1.4}_{-1.4} \times 10^{-6}$
	SBPL	$-1.0^{+0.3}_{-0.2}$	$-1.8^{+0.2}_{-0.3}$		150^{+70}_{-60}	383/479	$1.9^{+1.3}_{-0.7} \times 10^{-5}$

Table B6. Spectral analysis results for Interval 5 using *Fermi*-GBM detectors n7, n8, nb, and b1. The fluence is given in the 1–10 000 keV range. Uncertainties are given at the 90 per cent confidence level. For the NaI detectors, we use an energy range of 50–900 keV with the orbital background and 8–900 keV with the polynomial background. CPL is the preferred model with both the orbital and polynomial background.

Background	Model	α	β	E_p (keV)	kT (keV)	Stat/ DOF	Fluence (erg cm $^{-2}$)
Orbital	PL	$-1.286^{+0.013}_{-0.014}$				2331/395	$4.86^{+0.13}_{-0.13} \times 10^{-4}$
	BB				713^{+6}_{-6}	1155/395	$1.30^{+0.02}_{-0.02} \times 10^{-3}$
	CPL	$0.40^{+0.02}_{-0.02}$		3070^{+60}_{-60}		1117/394	$1.21^{+0.02}_{-0.02} \times 10^{-3}$
Polynomial	PL	$-1.17^{+0.02}_{-0.02}$				9296/482	$3.37^{+0.12}_{-0.13} \times 10^{-4}$
	CPL	$-0.71^{+0.03}_{-0.04}$		4700^{+600}_{-600}		9109/481	$5.1^{+0.2}_{-0.2} \times 10^{-4}$

Table B7. Spectral analysis results for Interval 6 using *Fermi*-GBM detectors n8, nb, and b1. The fluence is given in the 1–10 000 keV range. Uncertainties are given at the 90 per cent confidence level. For the NaI detectors, we use an energy range of 50–900 keV with the orbital background and 8–900 keV with the polynomial background. CPL is the preferred model with both the orbital and polynomial background.

Background	Model	$\alpha/$ $\alpha_1; \alpha_2$	β	E_p (keV)	E_b/kT (keV)	Stat/ DOF	Fluence (erg cm $^{-2}$)
Orbital	PL	$-1.51^{+0.03}_{-0.04}$				278/303	$6.3^{+0.6}_{-0.5} \times 10^{-5}$
	BB				$65.5^{+1.3}_{-1.3}$	458/303	$1.16^{+0.04}_{-0.04} \times 10^{-5}$
	CPL	$-1.14^{+0.06}_{-0.06}$		3400^{+900}_{-700}		226/302	$7.2^{+0.3}_{-0.4} \times 10^{-5}$
Polynomial	PL	$-1.37^{+0.03}_{-0.03}$				360/361	$5.9^{+0.3}_{-0.3} \times 10^{-5}$
	CPL	$-1.08^{+0.06}_{-0.07}$		2900^{+900}_{-700}		291/360	$5.7^{+0.3}_{-0.3} \times 10^{-5}$
	2SBPL	$-0.69^{+0.02}_{-0.02}; -1.27^{+0.05}_{-0.06}$	-6^{+3}_{-4}	3600^{+1300}_{-1300}	44^{+8}_{-7}	286/357	$6.0^{+0.7}_{-0.9} \times 10^{-5}$

Table B8. Spectral analysis results for Interval 7 using *Fermi*-GBM detectors n8, nb, and b1. The fluence is given in the 1–10 000 keV range. Uncertainties are given at the 90 per cent confidence level. For the NaI detectors, we use an energy range of 50–900 keV with the orbital background and 8–900 keV with the polynomial background. CPL is the preferred model with the orbital background. SBPL is the preferred model with the polynomial background.

Background	Model	α	β	E_p (keV)	E_b/kT (keV)	Stat/ DOF	Flux (erg cm $^{-2}$ s $^{-1}$)
Orbital	PL	$-1.50^{+0.02}_{-0.03}$				345/303	$1.6^{+0.2}_{-0.2} \times 10^{-4}$
	BB				$56.4^{+0.7}_{-0.7}$	697/303	$2.66^{+0.06}_{-0.07} \times 10^{-5}$
	CPL	$-1.24^{+0.04}_{-0.04}$		4300^{+1000}_{-800}		288/302	$1.79^{+0.07}_{-0.07} \times 10^{-4}$
	Band	$-1.24^{+0.04}_{-0.05}$	$-3.6^{+1.4}_{-6}$	4300^{+1100}_{-900}		288/301	$1.79^{+0.06}_{-0.06} \times 10^{-4}$
Polynomial	PL	$-1.36^{+0.02}_{-0.02}$				747/361	$1.52^{+0.06}_{-0.06} \times 10^{-4}$
	CPL	$-1.13^{+0.04}_{-0.04}$		3600^{+1000}_{-900}		657/360	$1.48^{+0.08}_{-0.08} \times 10^{-4}$
	SBPL	$-0.5^{+0.2}_{-0.2}$	$-1.60^{+0.05}_{-0.06}$		85^{+20}_{-14}	620/359	$1.19^{+0.08}_{-0.08} \times 10^{-4}$

Table B9. Spectral analysis results for the peak flux interval between T0+50,163.206 and T0 + 50,164.230 s using *Fermi*-GBM detectors n9, na, nb, and b1, and the Interval 3 orbital and polynomial backgrounds. The flux is given in the 1–10 000 keV range. Uncertainties are given at the 90 per cent confidence level. For the NaI detectors, we use an energy range of 75–900 keV with the orbital background and 75–900 keV with the polynomial background. CPL is the preferred model with both the orbital and polynomial background.

Background	Model	$\alpha/$ $\alpha_1; \alpha_2$	β	E_p (keV)	E_b/kT (keV)	Stat/ DOF	Flux (erg cm $^{-2}$ s $^{-1}$)
Orbital	PL	$-1.39^{+0.07}_{-0.08}$				197/366	$2.6^{+0.4}_{-0.4} \times 10^{-6}$
	BB				204^{+10}_{-11}	194/366	$1.26^{+0.10}_{-0.12} \times 10^{-6}$
	CPL	$-0.69^{+0.10}_{-0.12}$		3800^{+1200}_{-1100}		179/365	$3.8^{+0.3}_{-0.5} \times 10^{-6}$
	SBPL	$-0.93^{+0.09}_{-0.11}$	-7^{+3}_{-3}		7000^{+3000}_{-3000}	180/364	$4.1^{+0.4}_{-0.5} \times 10^{-6}$
	2SBPL	$2.65^{+0.04}_{-0.05}; -1.12^{+0.12}_{-0.2}$	-5^{+3}_{-5}	5000^{+3000}_{-2000}	133^{+8}_{-9}	180/362	$3.9^{+0.5}_{-0.5} \times 10^{-6}$
Polynomial	PL	$-1.42^{+0.07}_{-0.09}$				193/366	$2.4^{+0.3}_{-0.4} \times 10^{-6}$
	BB				140^{+7}_{-8}	199/366	$7.9^{+0.7}_{-0.8} \times 10^{-7}$
	CPL	$-0.93^{+0.11}_{-0.14}$		5000^{+2000}_{-2000}		184/365	$3.3^{+0.3}_{-0.6} \times 10^{-6}$

Table B10. Spectral analysis results for the peak flux interval between T0+59,024.082 and T0 + 59,025.106 s using *Fermi*-GBM detectors n8, nb, and b1, and the Interval 7 orbital and polynomial backgrounds. The flux is given in the 1–10 000 keV range. Uncertainties are given at the 90 per cent confidence level. For the NaI detectors, we use an energy range of 50–900 keV with the orbital background and 8–900 keV with the polynomial background. CPL is the preferred model with both the orbital and polynomial background.

Background	Model	α	β	E_p (keV)	E_b/kT (keV)	Stat/ DOF	Fluence (erg cm $^{-2}$)
Orbital	PL	$-1.43^{+0.08}_{-0.1}$				143/303	$2.5^{+0.5}_{-0.4} \times 10^{-6}$
	BB				89^{+5}_{-5}	149/303	$5.8^{+0.5}_{-0.6} \times 10^{-7}$
	CPL	$-1.01^{+0.13}_{-0.2}$		3000^{+2000}_{-2000}		133/302	$2.8^{+0.3}_{-0.4} \times 10^{-6}$
	Band	$-0.98^{+0.2}_{-0.2}$	$-2.8^{+0.8}_{-7}$	3000^{+2000}_{-2000}		133/301	$2.7^{+0.3}_{-0.4} \times 10^{-6}$
	SBPL	$-1.06^{+0.13}_{-0.2}$	$-2.5^{+0.6}_{-3}$		2000^{+2000}_{-1000}	133/301	$2.7^{+0.3}_{-0.3} \times 10^{-6}$
Polynomial	PL	$-1.33^{+0.06}_{-0.08}$				186/361	$2.4^{+0.3}_{-0.3} \times 10^{-6}$
	CPL	$-1.00^{+0.14}_{-0.2}$		3000^{+2000}_{-2000}		172/360	$2.5^{+0.3}_{-0.3} \times 10^{-6}$
	SBPL	$-0.8^{+0.2}_{-0.2}$	$-1.8^{+0.2}_{-0.5}$		400^{+200}_{-200}	171/359	$2.0^{+2}_{-0.6} \times 10^{-6}$

intervals during which *Fermi*-GBM was in a Target of Opportunity and then while *Fermi* was in a modified observing profile related to the stuck solar panel, thus the assumptions which underlie the orbital background tool are not necessarily met (G. Fitzpatrick et al. 2011). In their second fit interval, the change in the fit statistic between the PL and CPL model is significant according to the general GBM team criterion (e.g. S. Poolakkil et al. 2021). The reason for the lack of preference for turnover in their first interval is not immediately obvious.

B2.2 Konus-wind

We explore the spectral evolution of the burst using three-channel spectra, constructed from the counts in the G1, G2 and G3 energy bands. We select spectrum accumulation intervals corresponding to each separate emission episode determined using Bayesian blocks and peak flux intervals selected within each of the intervals. Because the emission is weak during Interval 3, there is no peak flux spectrum reported. The total time-integrated spectrum is constructed as a sum of counts in all episodes.

Details of the Konus-Wind three-channel spectral analysis can be found in (A. Tsvetkova et al. 2021). We perform the spectral analysis in XSPEC v.12.15.0 (K. Arnaud et al. 1999), using PL and CPL models parameterized by the peak energy of the $\nu F(\nu)$ spectrum and with the energy flux as the model normalization. Since a CPL fit to a three-channel spectrum has zero degrees of freedom (and, in the case of convergence, $\chi^2 = 0$), we do not report the statistic for such fits. We calculate the confidence intervals of the parameters using the command `steppar` in XSPEC.

B3 Quasi-periodic oscillations

For the cross-spectrum analysis we combine the G2 and G3 energy ranges and consider two independent observations from two Konus detectors, S1 and S2. The light curves are extracted with a binning of $\Delta t = 2.944$ s, and we compute power spectra using the `stingray` package over a continuous time interval 30 ks long, between T0+45,600 s and T0+75,600 s. We calculate the cross-power spectrum (CPS) between the two detectors using the combined G2 + G3 light curves, employing the `Crossspectr` class in `stingray` with Leahy normalization. The spectra are logarithmically rebinned in frequency space to reduce statistical scatter and enhance the visibility of broad features. An important

advantage of the CPS over individual power spectra is that white-noise contributions, being uncorrelated between detectors, do not contribute to the cross-spectrum. Possible detector-related systematics are likewise suppressed, removing the need for explicit modelling of these components.

To estimate the uncertainties on the CPS, we adopt a Monte Carlo approach. Specifically, we generate 1000 realizations of the light curves by varying the count rates in each time bin independently according to their measured variances. For each simulated light curve, we recompute the CPS, and from this ensemble we derive the mean and standard deviation of the power at each frequency. This procedure yields the statistical uncertainties on the measured CPS that serve as inputs to the subsequent fitting analysis.

The CPS is modelled using the sum of a power law and a Lorentzian component of the form

$$L(\nu) = \frac{A\gamma^2}{\gamma^2 + (\nu - \nu_0)^2} \quad (B7)$$

where ν_0 is the centroid frequency, γ is the full width at half-maximum, and A is the amplitude. In particular, noting a potentially interesting excess around 3 mHz, we perform a fit and summarize the best-fitting values in Table B11.

We compare the goodness of fit of a simple power-law model with a model including one Lorentzian component on top of the power law. To determine the significance of the improvement of the models over the null hypothesis of a power-law-only behaviour, we simulate 1000 CPS assuming the power-law-only best-fitting model and for each simulated CPS we perform the fit of the power-law-only (null-hypothesis) and the fit assuming the power-law + Lorentzian model (alternate hypothesis). As shown in Fig. B4, the observed $\Delta\chi^2$ values fall within the distribution expected from simulations under the null hypothesis, with p -values on the order of 10 per cent at most. No statistically significant features are found, and the inclusion of additional Lorentzian components does not improve the fit beyond the level expected from random fluctuations. We therefore conclude that there is no compelling evidence for QPOs in the CPS during this interval.

For the power spectrum analysis, we use the same time period (T0 + 45,600–75,600 s) and binning ($\Delta t = 2.944$ s) as in the CPS analysis. For each light curve of interest, we create a power spectral density (PSD) with the $(\text{rms}/\text{mean})^2$ normalization using the `pyLag` spectral-timing python package (D. R. Wilkins 2019). In this approach, we utilize the unbinned PSD to search for potential

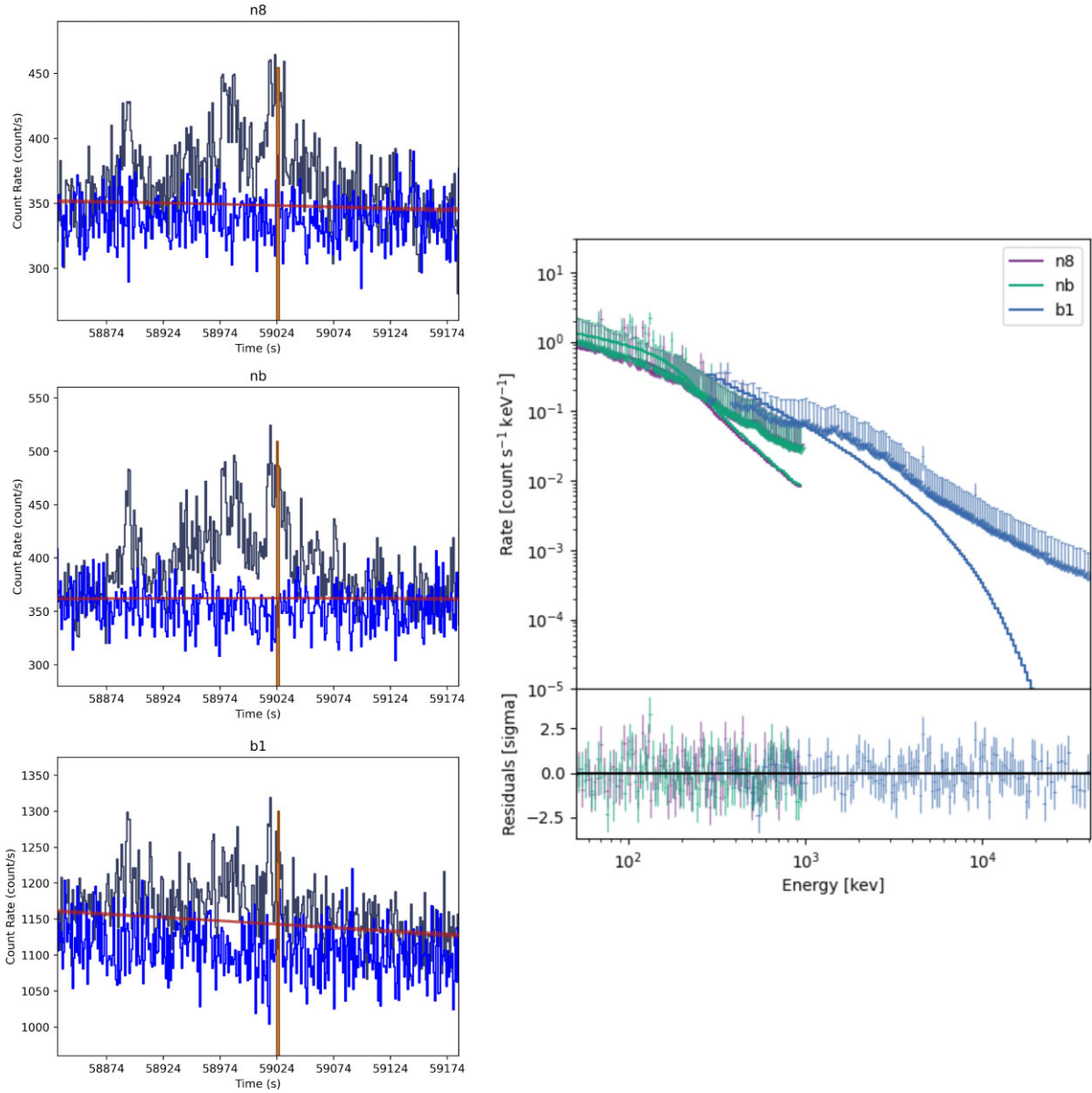


Figure B2. Spectral analysis results for the peak flux interval between $T_0 + 59,024.082$ and $T_0 + 59,025.106$ s using the orbital background estimation method. We use an energy range of 50–900 keV for the NaI detectors and 280 keV–40 MeV for the BGO detectors. *Left:* Light curves for each detector showing the signal during the GRB 250702B interval (black) with the peak flux interval shaded (light red), the raw orbital background (blue), and the polynomial fit to the orbital background and then normalized (red). *Right:* Count spectrum showing the CPL model fit to data.

QPOs, as has been commonly adopted in the search for QPOs around supermassive black holes (e.g. S. Vaughan 2005, 2010; M. Gierliński et al. 2008; W. N. Alston et al. 2014; M. Masterson et al. 2025). Each point in an unbinned PSD is distributed following a χ^2 distribution with two degrees of freedom (denoted χ^2_2 ; see S. Vaughan 2005, 2010 for more details). This distribution has a large variance compared to a Gaussian distribution, and hence, large fluctuations are relatively common and must be handled with statistical care.

To search for QPOs, we follow a maximum-likelihood approach, fitting the unbinned PSD using the Whittle likelihood given by

$$\ln \mathcal{L} = - \sum_j \left(\frac{I_j}{S_j} + \ln S_j \right), \quad (B8)$$

where j denotes a sum over all frequencies f_j , I_j is the observed power at frequency f_j , and S_j is the model power at frequency f_j .

For QPOs which appear as an excess in a single-frequency bin, the statistical significance of a single outlier bin can be estimated by measuring $T_R = \max_j R_j$, where $R_j = 2I_j/S_j$ (M. Gierliński et al. 2008; W. N. Alston et al. 2014). For QPOs which span multiple frequency bins, we must adopt a different approach that accounts for the spread of the power across many channels (see e.g. M. Masterson et al. 2025, for further discussion).

The Konus-Wind PSD for GRB250702B does not show any obvious single frequency channel outliers (i.e. $T_R \gtrsim 20$), but does show what looks like a potential broad feature around 3 mHz. Hence, we adopt the following approach to estimating the significance of this broad feature. We fit the data with two models: (1) a power-law plus constant model, where the constant accounts for the white noise at high frequencies, and (2) power-law plus constant plus Lorentzian, where the Lorentzian is to model a potential QPO. To compare these

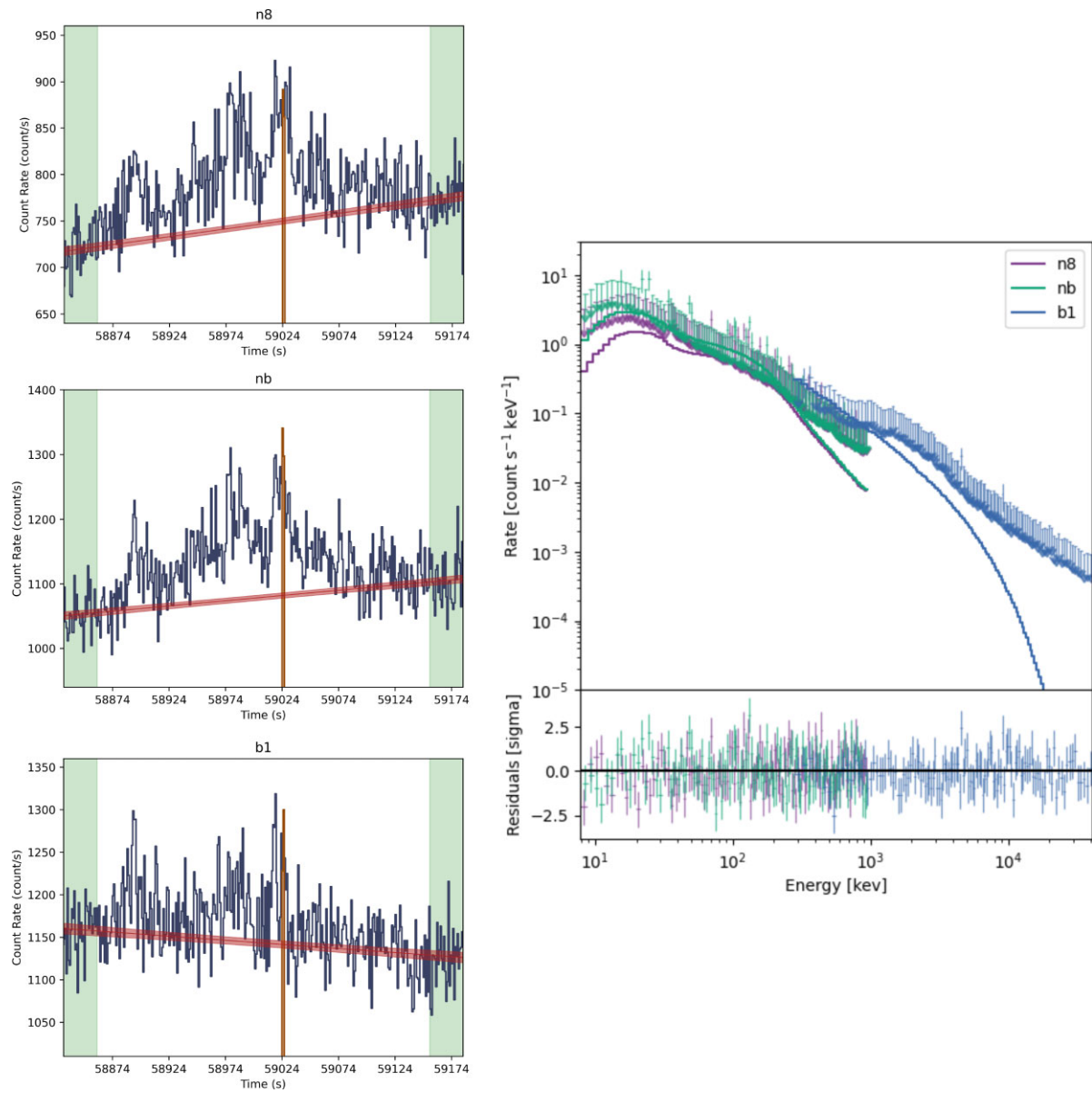


Figure B3. Spectral analysis results for the peak flux interval between $T_0 + 59,024.082$ and $T_0 + 59,025.106$ s using the polynomial background estimation method. We use an energy range of 8–900 keV for the NaI detectors and 280 keV–40 MeV for the BGO detectors. *Left:* Light curves for each detector showing the signal during the GRB 250702B interval (black) with the peak flux interval shaded (light red), the intervals in which the background polynomial is fit (green), and the polynomial fit (red). *Right:* Count spectrum showing the CPL model fit to data.

Table B11. Best-fitting parameters for power-law and power-law + Lorentzian models fit to the CPS. K is the power-law normalization and Γ is the power-law index.

Model	K	Γ	ν_0 (mHz)	γ (mHz)	A	χ^2/DOF
PL	0.007 ± 0.003	0.87 ± 0.06	–	–	–	462/64
PL + 1 $L(\nu)$ (high ν)	0.004 ± 0.003	0.92 ± 0.08	3.1 ± 0.3	1.1 ± 0.7	2.6 ± 1.2	405/61

two models, we compute the likelihood ratio test (LRT) statistic, given by $T_{\text{LRT}} = -2 (\ln \mathcal{L}_{H_0} - \ln \mathcal{L}_{H_1})$ (see Section 8 of S. Vaughan 2010, for more details), where H_0 indicates the power-law only model (the null hypothesis) and H_1 indicates the power-law plus Lorentzian model. Similar to the CPS analysis, we test the statistical significance of this additional model component by simulating 1000 realizations of the underlying broad-band noise and asking how often

an additional Lorentzian yields a comparable T_{LRT} . To simulate these realizations, we adopt the methodology outlined in J. Timmer & M. König (1995). In brief, this method takes an underlying PSD model and draws a normally distributed value for the real and imaginary part of the Fourier transform at each frequency that are proportional to the square root of the model power at that frequency. This method thus randomizes both the phase and the amplitude of the PSD,

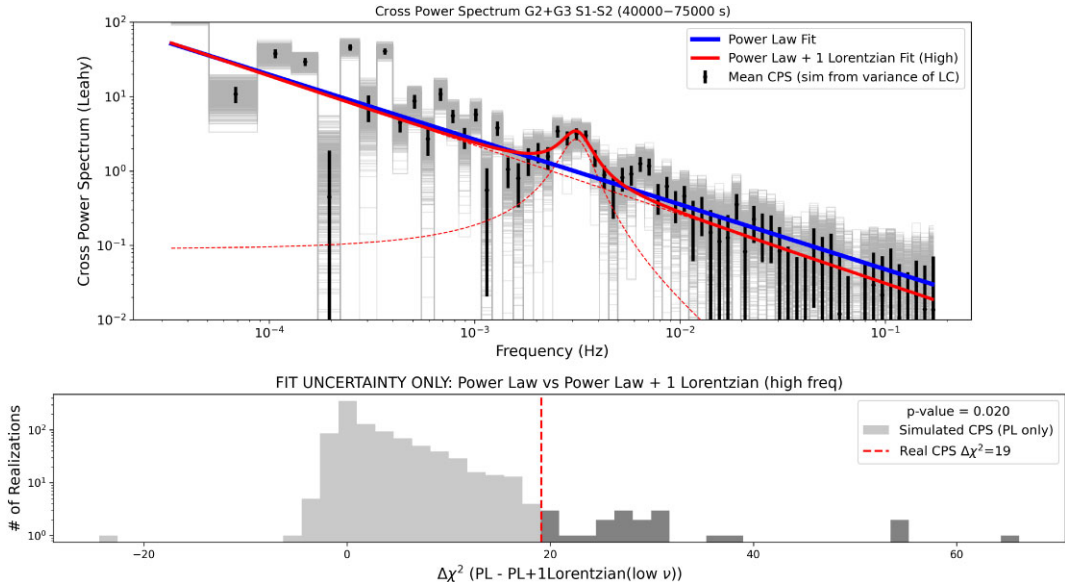


Figure B4. *Top:* CPS of G2+G3 S1-S2 in the interval $T_0 + 45\,600$ – $75\,600$ s. The grey lines show individual simulated CPS realizations derived by varying the individual time bins of the light curve according to the variance of the count rates, while the black points with error bars mark the mean CPS and their Gaussian standard deviations. The solid blue line represents the best-fitting power-law model. The red solid line corresponds to the power-law plus one Lorentzian (at high frequency) model. The dotted red lines show the individual power-law and Lorentzian components. *Bottom:* Distribution of simulated $\Delta\chi^2$ values obtained under the null hypothesis (power-law model only), compared with the observed data. Comparison between the power-law and power-law + Lorentzian models. The light grey histograms show the distribution from Monte Carlo simulations, while the dark grey regions indicate realizations with $\Delta\chi^2$ greater than or equal to the observed value. The dashed red line marks the $\Delta\chi^2$ measured from the real data, with the corresponding p -values reported in the legend.

correctly accounting for the χ^2 distribution of power that arises from summing in quadrature two normally distributed variables (the real and imaginary part of the Fourier transform). For each realization, we fit the simulated unbinned PSD with both models and record the T_{LRT} . We then adopt the ratio of simulations with T_{LRT} greater than the observed value to the total number of simulations as the resulting p -value for adding the Lorentzian component to the model.

The result of our PSD analysis is comparable that of the CPS; in short, we do not find any evidence for statistically significant ($> 3\sigma$) evidence for a QPO in the GRB250702B. We test many different combinations of Konus-Wind data, using the S2 detector and G2, G3, and G2 + G3 energy ranges. For each dataset, the best-fitting Lorentzian sits at around ~ 3 mHz, similar to what is seen in the CPS. In Fig. B5, we show an example of the PSD and best-fitting models for the S2, G2 + G3 data, along with the distribution of simulated T_{LRT} values. The resulting p -values for each energy range are: 0.030 (S2, G2), 0.5 (S2, G3), and 0.014 (S2, G2 + G3). Although the statistical significance can depend on the choice of broad-band noise model, we expect that any additional complexities in the model (e.g. a break in the power law) will only decrease the significance of a QPO-like feature. Hence, we find no strong evidence for a QPO in the Konus-Wind data of GRB 250702B.

B4 Bulk Lorentz factor

In order for the source to be optically thin to $\gamma\gamma$ -annihilation, in which the optical depth at a given energy $E_p < E < E_{\text{cut}}$ is $\tau_{\gamma\gamma}(\Gamma_0, E) < 1$, where E_{cut} is the cut-off energy, it must be moving ultrarelativistically with $\Gamma_0 \gg 1$ (M. G. Baring & A. K. Harding 1997; Y. Lithwick & R. Sari 2001; J. Granot et al. 2008; R. Hascoët et al. 2012).

In this case, the spectrum above E_{cut} will be optically thick to $\gamma\gamma$ -annihilation and will show either an exponential or a power-law

flux suppression (J. Granot et al. 2008). High-energy spectral cut-offs have been observed in several GRBs, e.g. GRB 090926A (M. Ackermann et al. 2011; M. Yassine et al. 2017), and GRBs 100724B and 160509A (G. Vianello et al. 2018, also see Q.-W. Tang et al. 2015 and L. Scotton et al. 2023 for additional sources), and were used to obtain an estimate of Γ_0 . When there is no clear high-energy spectral break and the emission is only seen up to a certain maximum energy, E_{max} , instead, then the same arguments can be used to place a lower limit on $\Gamma_0 > \Gamma_{0,\text{min}}$. Many works employ the one-zone assumption in which both the annihilating photons are co-spatial (e.g. Y. Lithwick & R. Sari 2001; A. A. Abdo et al. 2009). Such treatments yield an estimate of Γ_0 larger by a factor of ~ 2 than those that either consider two distinct emission zones (e.g. Y.-C. Zou, Y.-Z. Fan & T. Piran 2011) or account for the spatial, temporal, and directional dependence of the annihilating photons (J. Granot et al. 2008; R. Hascoët et al. 2012).

Here, we consider the analytic model of J. Granot et al. (2008) that assumes an ultrarelativistic thin spherical shell and calculates $\tau_{\gamma\gamma}$ along the trajectories of all observed photons to yield

$$\Gamma_0 = 100 \left[\frac{396.9}{C_2(1+z)^{\Gamma_{\text{ph}}}} \left(\frac{L_0}{10^{52} \text{ erg s}^{-1}} \right) \left(\frac{5.11 \text{ GeV}}{E_{\text{cut}}} \right)^{1+\Gamma_{\text{ph}}} \left(\frac{-\Gamma_{\text{ph}}}{2} \right)^{-5/3} \frac{33.4 \text{ ms}}{t_v} \right]^{1/(2-2\Gamma_{\text{ph}})} \quad (\text{B9})$$

where $L_0 = 4\pi d_L^2 (1+z)^{-\Gamma_{\text{ph}}-2} F_0$, t_v is the variability time-scale in milliseconds, Γ_{ph} is the photon index of the power-law spectrum at $E > E_{\text{pk}}$, F_0 is the (unabsorbed) energy flux (νF_ν) obtained at 511 keV from the power-law component, and d_L is the luminosity distance. The parameter $C_2 \approx 1$ is constrained from observations of spectral cut-offs in other GRBs (G. Vianello et al. 2018). R. Gill & J. Granot (2018) confirmed the results of this model by performing

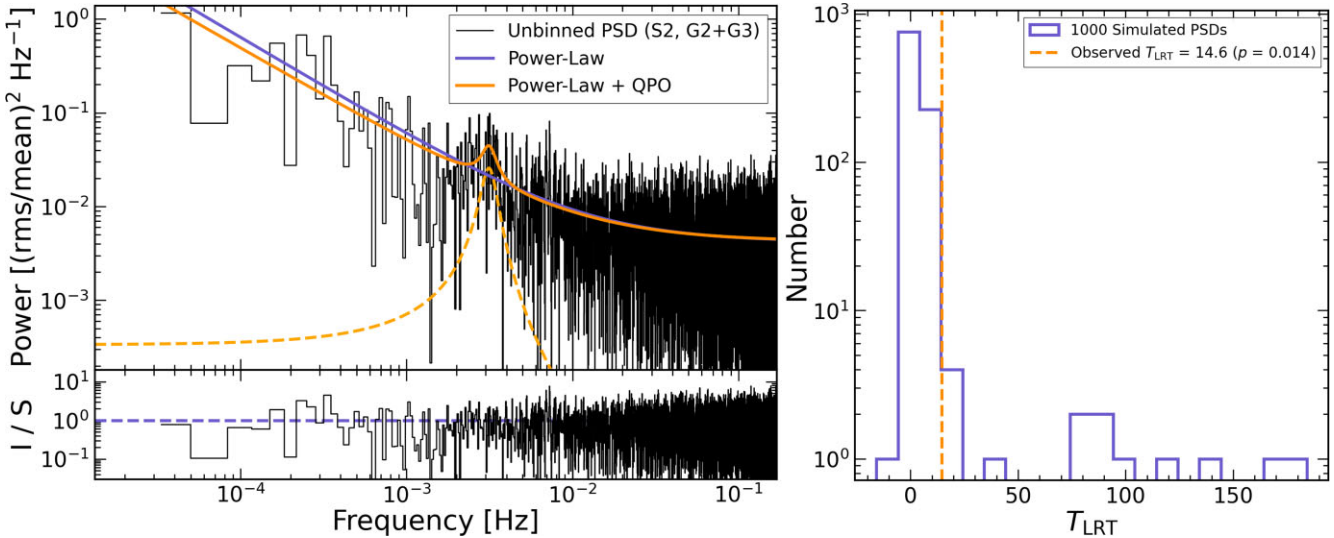


Figure B5. Example of PSD analysis for the S2, G2 + G3 data. *Left:* Unbinned PSD (black) from the S2, G2 + G3 data, fit with both a power-law plus constant model (purple) and a power-law plus constant plus Lorentzian model (orange). The bottom panel shows the data divided by the best-fitting power-law plus constant plus Lorentzian model. *Right:* The resulting T_{LRT} from adding a Lorentzian to the PSD model for 1000 simulated light curves with the same underlying power-law PSD. The dashed orange line shows the observed value of $T_{\text{LRT}} = 14.6$, which indicates a significance of $p = 0.014$.

numerical simulations, where they showed that it yields an accurate estimate of the bulk Lorentz factor from observations of spectral cut-offs if the emission region remains optically thin to Thomson scattering due to the produced e^\pm pairs.

The estimate of Γ_0 in equation B9 should be compared with $\Gamma_{0,\text{max}} = (1+z)E_{\text{cut}}/m_e c^2$, which is the maximum bulk Lorentz factor for a given E_{cut} and for which the cut-off energy in the comoving frame is at the self-annihilation threshold of $E'_{\text{cut}} = (1+z)E_{\text{cut}}/\Gamma_{0,\text{max}} = m_e c^2$. When the emission region is Thomson thick due to the created pairs, E'_{cut} can be slightly lower than $m_e c^2$ due to Compton downscattering (R. Gill & J. Granot 2018). When this is not the case, the true bulk Lorentz factor is obtained from the minimum of the two estimates.

For GBM Interval 7 of GRB 250702B, the MVT is ~ 1.4 s and the maximum observed photon energy is $E_{\text{max}} \sim 5$ MeV, with both parameters listed in the observer frame. Here, we consider two different spectral model fits, namely PL and CPL, that both yield an acceptable fit. The CPL model shows a spectral peak at $E_p \sim 4$ MeV, which we interpret as the high-energy spectral cut-off energy ($E_{\text{cut}} = E_{\text{peak}}$) with a hard photon index $\alpha = -1.24$ below this energy. For a photon flux of 2.9×10^{-4} ph/s/cm²/keV at $E = 511$ keV, we obtain an estimate of the true bulk Lorentz factor of $\Gamma_0 \simeq 81$ for the source redshift of 1.036. Alternatively, when considering the PL model that extends up to a maximum observed photon energy $E_{\text{max}} \sim 5$ MeV with photon index $\Gamma_{\text{ph}} = -1.50$, we constrain the bulk Lorentz factor from below and find $\Gamma_{0,\text{min}} \simeq 56$ for a photon flux of 2.2×10^{-4} ph s⁻¹ cm⁻² keV⁻¹. In this case, since there is no spectral information at $E > E_{\text{max}}$, we consider E_{max} as a lower limit on the photon energy of a possible high-energy spectral cut-off at some energy $E_{\text{cut}} > E_{\text{max}}$. For the same E_{cut} (E_{max}) in the CPL (PL) model, we find the maximum corresponding bulk Lorentz factor of $\Gamma_{0,\text{max}} \simeq 17$ (20).

When $\Gamma_{0,\text{max}}$ is smaller than Γ_0 or $\Gamma_{0,\text{min}}$, it implies a large Thomson optical depth due to the produced e^\pm -pairs, with $\tau_{T,\pm} \simeq 1.8 \times 10^4$ (2.8×10^3) for the cut-off power-law (power-law) model. R. Gill & J. Granot (2018) showed that in this case the spectrum above the peak energy of the Band spectrum would become hard

with photon index $\Gamma_{\text{ph}} \gtrsim -2$, as obtained in this GRB, which would manifest as a flat or slightly rising spectrum in νF_ν above E_p with a sharp spectral cut-off at $E'_{\text{cut}} < m_e c^2$ in the comoving frame. In this situation, $\Gamma_{0,\text{max}}$ would underpredict the true bulk Lorentz factor by up to a factor of ten, and the true Lorentz factor is much closer to Γ_0 or $\Gamma_{0,\text{min}}$ when calculated using equation B9, which we adopt here.

The coasting bulk Lorentz factor of the ejecta can also be inferred from the afterglow when the light curve shows a clear deceleration peak, e.g. in the optical and/or X-rays, which are often located between the injection and cooling break frequencies, ν_m and ν_c , respectively, of the slow-cooling synchrotron spectrum. Then, depending on the power-law index, p , of the energy distribution of the radiating electrons, $N_e(\gamma) \propto \gamma^{-p}$ for $\gamma > \gamma_m$, and the radial profile of the external medium density, $n_{\text{ext}} = n_0(R/R_0)^{-k}$, the afterglow flux density declines at $T > T_{\text{dec}}$ as a power law with $d \ln F_\nu / d \ln T = [k(3p - 5) - 12(p - 1)]/4(4 - k)$.

In the thin-shell approximation, $T_{\text{dec}} = (1+z)[(3-k)E_{\text{k,iso}}/2^{5-k}\pi A c^{5-k} \Gamma_0^{2(4-k)}]^{1/(3-k)}$ marks the time at which the flow decelerates by sweeping up mass $M_{\text{sw}}(R) = 4\pi\rho(R)R^3/(3-k) = M_0/\Gamma_0 = E_{\text{k,iso}}/\Gamma_0^2 c^2$ in the external medium, where $\rho(R) = m_p n_{\text{ext}}(R) = A R^{-k}$ and M_0 is the mass of the ejecta. No afterglow light curve peak in the optical and X-rays was seen in GRB 250702B and all of the observations were obtained post-deceleration, so only a lower limit can be placed on Γ_0 . In fact, the afterglow modelling in A. J. Levan et al. (2025a) suggests that the steeply decaying X-ray and optical afterglow observations were made after an early jet break at $T_{\text{jet}} \lesssim 0.5$ d and where the jet propagates inside a wind ($k = 2$) medium. Therefore, $T_{\text{dec}} < T_{\text{jet}}$, which yields $\Gamma_0 \gtrsim 23(1+z)^{1/4} E_{\text{k,iso},54} A_*^{-1/4} T_{\text{jet},4}^{-1/4}$ for $k = 2$ and $A = 3 \times 10^{35} A_* \text{ cm}^{-1}$. This lower limit is consistent with the estimate of the bulk Lorentz factor obtained above.

These values are broadly consistent with measurements from multiwavelength afterglow modelling. A. J. Levan et al. (2025a) infer a bulk Lorentz factor at ~ 0.5 day of ~ 40 , which would be lower than the initial value due to deceleration. B. O'Connor et al. (2025) measure a comparable Γ_0 . With the additional restriction of $\Gamma_0 \theta_j \geq 1$, with θ_j the half-jet opening angle, to prevent the jet from

spreading laterally in the coasting phase they measure $\Gamma_0 \gtrsim 100$. Thus, all approaches require an ultrarelativistic jet.

APPENDIX C: DETAILED DISCUSSION ON EXCLUDED PROGENITORS

The following subsections discuss each physical progenitor in detail, and why it is excluded. Beyond the progenitor systems discussed below, there are two possible options to explain the extreme duration as arising not from intrinsic accretion time-scales but from propagation effects. One is the option of a lensed event, where the duration arises from seeing temporally delayed lenses. While this could, in principle, explain the gamma-ray signature, it is not compatible with the \sim day earlier signal seen only in X-rays. The other option is dust echoes of the initial signal from surrounding material in the host galaxy. However, this should be negligible above ~ 100 keV, which is incompatible with our observation of multiple MeV photons in late pulses, as noted in A. J. Levan et al. (2025a).

C1 X-ray binaries (and other galactic sources)

Early on in the study of this event, the alignment with the Galactic plane suggested a possible source within the Milky Way. Many Galactic sources which involve compact objects produce flares which are recovered in the GRB monitors. As one particular example, we highlight X-ray binaries. These are binary systems where a compact object accretes material from a donor star. This can launch jets which have been observed with \sim week durations in the GRB monitors (e.g. P. Jenke et al. 2016). However, it is rare for X-ray binaries (and other Galactic sources) to exceed being detected to a few hundred keV, and none have been seen to 5 MeV. To this we add the 0.05 per cent chance alignment with the extragalactic putative host galaxy (A. J. Levan et al. 2025a).

C2 Magnetar giant flares

Magnetars are neutron stars with the most extreme persistent magnetic fields in the cosmos (C. Thompson & R. C. Duncan 1995). These sources produce flares, the most extreme of which are giant flares, observed up to MeV energies and seen in the Milky Way and other nearby galaxies (E. Burns et al. 2021; M. Negro et al. 2024). However, their emission size is comparable to the size of a neutron star, with durations of the prompt spike lasting fractions of a second. The duration is inconsistent by orders of magnitude.

C3 Neutron star mergers

Neutron star mergers refer to both binary neutron star and neutron star-black hole mergers. In either scenario, the accretion time-scale is on the order of 0.1 s, suggesting prompt durations under 10 s in duration (C. L. Fryer et al. 2019). However, short GRBs with extended emission have properties expected from a compact merger origin, and have durations up to ~ 100 s (J. P. Norris & J. T. Bonnell 2006). Further, recent works have identified long-duration GRBs which must arise from merger events due to offsets from their host galaxies (J. C. Rastinejad et al. 2022; B. P. Gompertz et al. 2023; A. J. Levan et al. 2024) and may arise from neutron star mergers. These bursts also reach ~ 100 s in duration. Thus, neutron star mergers are inconsistent in duration by orders of magnitude.

C4 White dwarf mergers

White dwarfs merging with other stellar remnants (white dwarf, neutron star, black hole) have been discussed as possible GRB progenitors. We first note that it is not guaranteed that these mergers will produce jets. White dwarf-white dwarf binaries can produce a wide variety of explosions including thermonuclear (type Ia) supernovae and short-duration GRBs assuming the collapse of white dwarfs with strong magnetic fields (J. A. Rueda et al. 2023; P. C.-K. Cheong et al. 2025). White dwarf-neutron star and white dwarf-black hole mergers have been proposed for a wide range of peculiar supernova explosions (B. D. Metzger 2012; M. A. R. Kaltenborn et al. 2023). None of these signatures have ever been associated with GRBs.

However, if we assume such mergers produce ultrarelativistic jets, stellar remnant merger options involving one white dwarf are the most natural to explain ultra-long GRBs. This is because, compared to neutron stars and black holes, white dwarfs have large radii: $\sim 3 \times 10^8$ cm for a white dwarf near the Chandrasekhar limit and 10^9 cm for a $0.5 M_\odot$ white dwarf. The corresponding orbital separation when the white dwarf overfills its Roche limit is $(1-5) \times 10^9$ cm. The specific angular momentum from these mergers is $7 \times 10^{17} - 3 \times 10^{18}$ cm/s, higher than most collapsar progenitors. Simulations of these mergers showed high accretion rates for 15–150 s (C. L. Fryer et al. 1999), but the disc formed in these mergers could continue to accrete for up to 10 000 s for an α -disc model where the viscous $\alpha \approx 0.01$. The duration does not increase dramatically with increasing compact remnant mass so we would expect the same durations for IMBHs. The accretion rate drops considerably after the first 100 s, making a strong long-duration jet unlikely. Given the \sim day lead up to the strongest signal in GRB 250702B, these models are excluded.

C5 Relativistic tidal disruption event

TDEs occur when a star encounters a massive black hole and is disrupted when the gravitational gradient of the black hole overcomes the binding energy of the star. These events are commonly detected and studied in optical and X-ray wavelengths. A rare subset of TDEs occur when the accretion onto the black hole generates a relativistic jet. Four events are known, of which three were discovered by the *Swift*-BAT and seen in hard X-rays for a few days (H. Krimm et al. 2011a, b; T. Sakamoto et al. 2011; I. Andreoni et al. 2022). For these reasons, relativistic TDEs are a viable model for ultra-long GRBs, and are thus an attractive model to consider for GRB 250702B.

We find TDEs involving a massive black hole to be incompatible with the gamma-ray results for GRB 250702B. First, we note only one relativistic TDE has ever reached the onboard trigger threshold of a GRB monitor. Further, none have been observed above a few hundred keV, let alone several MeV. And of the relativistic TDEs seen in gamma-rays and followed in X-rays, their durations are more than an order of magnitude longer than the emission in GRB 250702B. Near-infrared observations show GRB 250702B to be non-nuclear in the host galaxy, while nearly all TDEs arise from nuclear positions (A. J. Levan et al. 2025a).

For better comparison, we repeat our MVT analysis procedure using a *Swift*-BAT mask-weighted light curve in 1 ms bins for *Swift* J1644+57 (D. N. Burrows et al. 2011), the relativistic TDE with the shortest known variation time-scale, finding a value of ~ 54 s. With a redshift of 0.33 (A. J. Levan et al. 2011), this corresponds to a rest-frame MVT of ~ 40 s. Taking the Schwarzschild crossing time limit, this corresponds to a black hole mass of a few million solar masses, matching the results of X-ray reverberation

mapping (E. Kara et al. 2016). Further, the physical scales involved in TDEs are expected to be orders of magnitude larger than the Schwarzschild light crossing time on both analytic grounds and results from simulations (M. J. Rees 1988; S. Ayal, M. Livio & T. Piran 2000). This led some to invoke a white dwarf merging with an IMBH for *Swift* J1644 + 57 (J. H. Krolik & T. Piran 2011).

C6 Intermediate-mass black hole tidal disruption event

In principle, an IMBH may resolve the issues with a relativistic TDE. Indeed A. J. Levan et al. (2025a) invoke this as a viable model, highlighting it also explains the non-nuclear origin of the transient with respect to the host galaxy. However, there are multiple difficulties with this model which are discussed in the text.

C7 Typical (carbon–oxygen) collapsar

Most long GRBs arise from a collapsar origin. Theoretically, this is a rapidly rotating compact star which results in strong accretion after core-collapse (A. I. MacFadyen & S. E. Woosley 1999). This powers bipolar ultrarelativistic jets which produce the prompt and afterglow signatures. The shockwave generated as the jet propagates through the star in concert with the winds from the accretion disc explode the star, powering a supernova, which is also regularly observed. Observationally, effectively all supernovae seen following long GRBs are type Ic broad-line (Z. Cano et al. 2017). The concordance model from theory and simulation is collapsar GRBs arise from the deaths of rapidly rotating stars which have been stripped of both hydrogen and helium, i.e. carbon–oxygen stars.

This origin is well matched to the properties of GRB 250702B. It explains the relativistic jets and the follow-up data showing both a consistency with an external shock as well as the transient occurring within the stellar field of the host galaxy (A. J. Levan et al. 2025a). The long GRB population has typical MVT values (or upper limits) of $\sim 0.1\text{--}10$ s and peak energies from a few tens to hundreds of keV (S. Poolakkil et al. 2021; P. Veres et al. 2023). The values of GRB 250702B are well within the known populations for these parameters.

However, the prompt duration is far too long. The duration of the prompt GRB emission is determined by how long internal dissipation occurs in the jet. This is then tied to the accretion time-scale on to the central engine. As discussed in Section 5, the total accretion time-scale is a combination of the free-fall time-scale for the material to hang up in a disc and then the disc accretion time-scale. For systems spun up by tides from tight binaries, the angular momentum (shown in Fig. 5) is only sufficient to form a fairly compact disc (1000–10 000 km). With these models, it is difficult to produce accretion time-scales that exceed a few thousand seconds (Fig. 7 shows a carbon–oxygen binary where the orbital separation is at the Roche limit). The corresponding luminosity for our $32 M_{\odot}$ progenitor in a tight binary is shown in Fig. 7. C. L. Fryer et al. (2025) explore the maximal duration viable through stars spun up near breakup by a tight binary for a broad number of stellar systems finding maximal accretion time-scales of ~ 1000 s. Even allowing for extension of this time-scale due to different engine models or due to observing the emitting region (not the accretion itself), this is incompatible with the total $\sim 100 000$ s duration of GRB 250702B.

C8 Helium collapsars

A collapsar from a helium star progenitor may extend the duration because the larger radius leads to a longer freefall time. C. L. Fryer

et al. (2025) also studied tidally spun-up helium star binaries. In general, the angular momentum at any given mass coordinate for a helium-star binary is lower than that of a carbon–oxygen binary. In addition, only the tightest of helium-star binaries have sufficient angular momentum to form a disc. Figs 5 and 6 show the angular momentum and accretion time-scales for helium star binaries with orbital separations at the Roche limit. The corresponding jet power is shown in Fig. 7. The lower angular momentum means that the jet power peaks early and decays earlier. But the helium collapsar has additional material (in the helium envelope) that can produce long-term accretion that extends beyond that of a typical carbon–oxygen collapsar. At these late times, the luminosity has already dropped considerably, over two orders of magnitude below peak. Thus, helium collapsars cannot explain the gamma-ray duration.

C9 Supergiant collapsars

Blue supergiants were invoked to explain the extreme duration of GRB 111209A (B. Gendre et al. 2013; K. Ioka, K. Hotokezaka & T. Piran 2016; R. Perna, D. Lazzati & M. Cantiello 2018). However more than a decade later, no viable mechanism to achieve sufficient rotation in the progenitor star has been identified. Even if we assume mild coupling between burning layers, the maximum accretion time-scale will be determined by the free-fall time on to the disc. For example, using equation 1, the accretion time-scale for a 10^{12} cm, $40 M_{\odot}$ blue supergiant would be 15 000 s, insufficient for the duration of GRB 250702B. Further, such events would likely have the strongest accretion at early times, in contrast to what is seen for GRB 250702B. Thus, this model is excluded.

C10 Collapsar with magnetar central engine

Magnetar central engines are sometimes invoked to explain specific observational signatures seen in GRBs, such as plateaus following short GRBs (B. Gompertz, P. O’Brien & G. Wynn 2014). However, they are disfavoured as viable engines for collapsar GRBs for both observational and theoretical reasons. Observationally, collapsar GRBs arise predominantly from low-metallicity galaxies (A. Fruchter et al. 2006). This was confirmation of a prediction from early theoretical papers (e.g. A. I. MacFadyen & S. E. Woosley 1999) where the low metallicity is a requirement to form the black hole to power the jet. Higher metallicity star forming regions produce fewer large stars, and the large stars they do produce still end as neutron stars because of significant mass-loss through winds. Magnetars are thus not important contributors to the long GRB population (C. L. Fryer et al. 2025). Further, in core-collapse supernovae, even if the stellar remnant forms an extreme magnetic field, it will be buried for decades to a millennia (R. A. Chevalier 1989; U. Geppert, D. Page & T. Zannias 1999), precluding tapping of the magnetic fields to drive the relativistic jets. Even if we ignore these problems and treat ultralongs as somehow arising from magnetar central engines, the kinetic energy extracted from the rotation of the magnetar would peak at early times and decay as a power law in time. Thus, the delayed peak in GRB 250702B is incompatible with a magnetar central engine.

C11 Binary helium star merger

The merger of two evolved cores (e.g. two helium cores) has also been invoked as a means to produce a spun up core prior to collapse. Detailed studies of these mergers found that, although the merged system had more angular momentum than typical single-star models, they did not produce systems spinning more rapidly than tidally spun

up models (C. L. Fryer & A. Heger 2005). Unless the collapse occurs shortly after the merger, these systems will likely have durations that are shorter than tidally spun-up systems. Even if the collapse occurs right after the merger, the peak accretion rates and jet powers will occur well below a few thousand seconds. These events are thus also inconsistent with the observed duration in GRB 250702B.

¹Department of Physics, The George Washington University, 725 21st St NW, Washington, DC 20052, USA

²Astrophysics Science Division, NASA Goddard Space Flight Center, 8800 Greenbelt Road, Greenbelt, MD 20771, USA

³Department of Physics & Astronomy, Louisiana State University, Baton Rouge, LA 70803, USA

⁴Center for Theoretical Astrophysics, Los Alamos National Laboratory, Los Alamos, NM 87545, USA

⁵Ioffe Institute, Polytekhnicheskaya, 26, Saint Petersburg 194021, Russian Federation

⁶Science and Technology Institute, Universities Space Research Association, Huntsville, AL 35805, USA

⁷Instituto de Radioastronomía y Astrofísica, Universidad Nacional Autónoma de México, Antigua Carretera a Pátzcuaro # 8701, Ex-Hda. San José de la Huerta, Morelia C.P. 58089, Michoacán, México

⁸Astrophysics Research Center of the Open University (ARCO), The Open University of Israel, PO Box 808, Ra'anana 4353701, Israel

⁹MIT Kavli Institute for Astrophysics and Space Research, Massachusetts Institute of Technology, Cambridge, MA 02139, USA

¹⁰Department of Astronomy and Astrophysics, The Pennsylvania State University, 525 Davey Lab, University Park, PA 16802, USA

¹¹Institute for Gravitation and the Cosmos, The Pennsylvania State University, University Park, PA 16802, USA

¹²Johns Hopkins University Applied Physics Laboratory, Laurel, MD 20723, USA

¹³School of Physics, Engineering and Technology, University of York, Heslington, York YO10 5DD, UK

¹⁴Department of Physical Science, Aoyama Gakuin University, 5-10-1 Fuchi-nobe, Chuo-ku, Sagamihara, Kanagawa 252-5258, Japan

¹⁵Department of Natural Sciences, The Open University of Israel, PO Box 808, Ra'anana 4353701, Israel

¹⁶Astrophysics Research Institute, Liverpool John Moores University, IC2 Liverpool Science Park, 146 Brownlow Hill, Liverpool L3 5RF, UK

¹⁷ST12 Astrophysics Branch, NASA Marshall Space Flight Center, Huntsville, AL 35812, USA

¹⁸Department of Physics, Brown University, Providence, RI 02912, USA

¹⁹Center for Astrophysics | Harvard & Smithsonian, 60 Garden Street, Cambridge, MA 02138-1516, USA

²⁰The NSF AI Institute for Artificial Intelligence and Fundamental Interactions, Cambridge, MA 02138, USA

²¹Istituto Nazionale di Fisica Nucleare, Sezione di Bari, I-70126 Bari, Italy

²²Università degli studi di Trento, via Calepina 14, I-38122 Trento, Italy

²³Amenum Space Exploration Division, Huntsville, AL 35806, USA

²⁴Center for Space Plasma and Aeronomics Research, University of Alabama in Huntsville, Huntsville, AL 35899, USA

²⁵Dipartimento Interateneo di Fisica, Politecnico di Bari, Bari, Italy

²⁶Department of Space Science, University of Alabama in Huntsville, 320 Sparkman Drive, Huntsville, AL 35899, USA

²⁷Max-Planck-Institut für extraterrestrische Physik, Giessenbachstrasse 1, D-85748 Garching, Germany

²⁸Department of Aerospace, Physics and Space Sciences, Florida Institute of Technology, Melbourne, FL 32901, USA

²⁹INAF – Osservatorio Astronomico di Roma, Via Frascati 33, I-00078 Monteporzio Catone (RM), Italy

³⁰Gran Sasso Science Institute (GSSI), I-67100 L'Aquila, Italy

³¹NASA Postdoctoral Program Fellow, NASA Marshall Space Flight Center, Huntsville, AL 35812, USA

³²Department of Physics, University of Cagliari, SP Monserrato-Sestu, km 0.7, I-09042 Monserrato, Italy

³³Department of Physics and Astronomy, Northwestern University, Evanston, IL 60208, USA

³⁴Center for Interdisciplinary Exploration and Research in Astronomy (CIERA), Northwestern University, 1800 Sherman Avenue, Evanston, IL 60201, USA

This paper has been typeset from a TeX/LaTeX file prepared by the author.